USGS
science for a changing world

System Characterization Report on the Environmental Mapping and Analysis Program (EnMAP)

Chapter S of
System Characterization of Earth Observation Sensors

Open-File Report 2021–1030–S

U.S. Department of the Interior
U.S. Geological Survey

System Characterization Report on the Environmental Mapping and Analysis Program (EnMAP)

By Minsu Kim,[1] Seonkyung Park,[2] and Cody Anderson[3]

Chapter S of
System Characterization of Earth Observation Sensors

Compiled by Shankar N. Ramaseri Chandra[1]

[1]KBR, Inc., under contract to the U.S. Geological Survey.

[2]USS, Inc., under contract to the U.S. Geological Survey.

[3]U.S. Geological Survey.

Open-File Report 2021–1030–S

U.S. Department of the Interior
U.S. Geological Survey

U.S. Geological Survey, Reston, Virginia: 2025

Suggested citation:
Kim, M., Park, S., and Anderson, C., 2025, System characterization report on the Environmental Mapping and Analysis Program (EnMAP), chap. S *of* Ramaseri Chandra, S.N., comp., System characterization of Earth observation sensors: U.S. Geological Survey Open-File Report 2021–1030, 28 p., https://doi.org/10.3133/ofr20211030S.

ISSN 2331-1258 (online)

Contents

Figures

Tables

Conversion Factors

International System of Units to U.S. customary units

Multiply	By	To obtain
	Length	
nanometer (nm)	3.93701×10^{-8}	inch (in.)
micrometer (μm)	3.9370×10^{-5}	inch (in.)
meter (m)	3.281	foot (ft)
meter (m)	1.094	yard (yd)
kilometer (km)	0.6214	mile (mi)

Abbreviations

B2B	band to band
CHISQ	chi-squared
ECCOE	Earth Resources Observation and Science Cal/Val Center of Excellence
EnMAP	Environmental Mapping and Analysis Program
FWHM	full width at half maximum
GSD	ground sample distance
I2I	image to image
JACIE	Joint Agency Commercial Imagery Evaluation
OLI	Operational Land Imager
RadCalNet	Radiometric Calibration Network
SR	surface reflectance
SWIR	shortwave infrared
TOA	Top of Atmosphere
TOAR	Top of Atmosphere reflectance
USGS	U.S. Geological Survey
VNIR	visible and near infrared

System Characterization Report on the Environmental Mapping and Analysis Program (EnMAP)

By Minsu Kim,[1] Seonkyung Park,[2] and Cody Anderson[3]

Executive Summary

This report addresses system characterization of the Environmental Mapping and Analysis Program hyperspectral sensor by the DLR (German Aerospace Center, ground segment project management), GFZ (Deutsches Geoforschungszentrum, science lead) and is part of a series of system characterization reports produced and delivered by the U.S. Geological Survey Earth Resources Observation and Science Cal/Val Center of Excellence. These reports present and detail the methodology and procedures for characterization; present technical and operational information about the EnMAP hyperspectral sensor; and provide a summary of test measurements, data retention practices, data analysis results, and conclusions.

The Earth Resources Observation and Science Cal/Val Center of Excellence system characterization team completed data analyses to characterize the geometric (interior and exterior), and radiometric performances of the EnMAP hyperspectral sensor. Results of these analyses indicate that the Environmental Mapping and Analysis Program has a band-to-band geometric performance in the range of −0.135 to 0.15 pixel, geometric performance relative to the Operational Land Imager in the range of −27.716 meters (−0.92 pixel) to 32.892 meters (1.09 pixels) offset in comparison to Landsat 8 Operational Land Imager, offset of a radiometric comparison in the range of −0.012 to 0.020, slope of a radiometric comparison in the range of 0.947 to 1.031.

Introduction

This section describes the basic information of the sensor and its scientific goals and the scope of system characterization analysis.

Background

The Environmental Mapping and Analysis Program (EnMAP) is a hyperspectral electro-optical instrumentation that analyzes the chemical-physical composition of the objects present in a scene (EnMAP, 2024). EnMAP offers the scientific community and users many applications in the fields of environmental monitoring, resource management, crop classification, pollution control, and others. The mission objective is to provide a global observation capability with the specific areas of interest over Europe and the Mediterranean region.

The data analysis results provided within this report have been derived from approved Joint Agency Commercial Imagery Evaluation (JACIE) processes and procedures (Cantrell and Christopherson, 2024). The JACIE was formed to leverage resources from several Federal agencies for the characterization of remote sensing data and to share those results across the remote sensing community. More information about JACIE is available at https://www.usgs.gov/calval/jacie.

Purpose and Scope

The purpose of this report is to describe the EnMAP hyperspectral sensor, test its performance in three categories, complete related data analyses to quantify these performances, and report the results in a standardized document. The performance testing of the system is limited to geometric and radiometric analyses. The scope of the geometric assessment is limited to testing the interior alignments of spectral bands against each other, and the exterior alignment is tested in reference to the Landsat 8 Operational Land Imager (U.S. Geological Survey, 2025).

The U.S. Geological Survey (USGS) Earth Resources Observation and Science Cal/Val Center of Excellence (ECCOE; U.S. Geological Survey, 2020) and the associated system characterization process used for this assessment follows the USGS Fundamental Science Practices, which include maintaining data, information, and documentation needed to reproduce and validate the scientific analysis documented in this report. Additional information and guidance about Fundamental Science Practices and related

[1]KBR, Inc., under contract to the U.S. Geological Survey.

[2]USS, Inc., under contract to the U.S. Geological Survey.

[3]U.S. Geological Survey.

resource information of interest to the public are available at https://www.usgs.gov/about/organization/science-support/office-science-quality-and-integrity/fundamental-science-practices. For additional information related to the report, please contact ECCOE at eccoe@usgs.gov.

System Description

This section describes the satellite and operational details and provides information about the EnMAP hyperspectral sensor.

Satellite and Operational Details

The satellite and operational details for EnMAP are listed in table 1.

Sensor Information

The imaging sensor details for EnMAP are listed in table 2. The spectral resolution of each band is 12 nanometers for full width at half maximum (FWHM).

Table 1. Satellite and operational details for the Environmental Mapping and Analysis Program.

[°, degree; ±, plus or minus; m, meter]

Product information	EnMAP
Satellite and operational information	
Sensor name(s)	EnMAP
Sensor type	Hyperspectral
Mission type	Global land-monitoring mission
Launch date	April 1st, 2022
Expected lifetime	5 years
Operational details	
Operating orbit	Sun-synchronous orbit
Orbital altitude range	653 km
Sensor angle altitude	97.96° inclination
Imaging time	11:18 a.m. (local time)
Geographic coverage	30 km (field of view, 2.63°)
Temporal resolution	27 days
Temporal coverage	2022 to present
Imaging angles	±30°
Ground sample distance(s)	30 m
Product abstract	https://www.enmap.org

Table 2. Imaging sensor details for the Environmental Mapping and Analysis Program.

[µm, micrometer; GSD, ground sample distance; m, meter; VNIR, visible and near infrared; SWIR, shortwave infrared]

Spectral band details	EnMAP			
	Lower band (µm)	Upper band (µm)	Radiometric resolution (bits)	GSD (m)
VNIR (91 channels)	0.418	0.993	13	30.0
SWIR (133 channels)	0.902	2.446	14	30.0

Procedures

The ECCOE has established standard processes to identify Earth observing systems of interest and to assess the geometric and radiometric qualities of data products from these systems (Cantrell and Christopherson, 2024).

The assessment steps are as follows:

- system identification and investigation to learn the general specifications of the satellite and its sensor(s);
- data receipt and initial inspection to understand the characteristics and any overt flaws in the data product so that it may be further analyzed;
- geometric characterization, including interior geometric orientation measuring the relative alignment of spectral bands and exterior geometric orientation measuring how well the georeferenced pixels within the image are aligned to a known reference; and
- radiometric characterization, including assessing how well the data product correlates with a known reference and, when possible, assessing the signal-to-noise ratio.

The specific procedures required to handle hyperspectral data are as follows:

- correction of defective pixel that causes a dark striping;
- spectral resampling of hyperspectral data to match the spectral response function of Landsat 8 Operational Land Imager (OLI); and
- computation of solar irradiance by resampling high resolution extraterrestrial solar irradiance based on spectral response function of Landsat 8 OLI.

Data analysis and test results are maintained at the USGS Earth Resources Observation and Science Center by the ECCOE project.

Measurements

The observed USGS measurements are listed in table 3. Details about the methodologies used are outlined in the "Analysis" section.

Table 3. U.S. Geological Survey measurement results.

[nm, nanometer; RMSE, root mean square error; OLI, Operational Land Imager; m, meter; R^2, coefficient of determination; %, percent; RER, relative edge response; FWHM, full width at half maximum; MTF, modulation transfer function]

Description of product	System characterization results
Geometric performance (easting, northing), in meters (pixels)	
Band to band (571 nm reference, band 31)	Mean: −0.052 to 0.150 pixel, −0.135 to 0.093 pixel RMSE: 0.089 to 0.315 pixel, 0.080 to 0.419 pixel
Image to image (against OLI)	Easting mean: −27.716 to −18.892 m (−0.92 to −0.63 pixel) Easting RMSE: 19.517 to 28.375 m (0.65 to 0.95 pixel) Northing mean: 15.307 to 32.892 m (0.51 to 1.09 pixels) Northing RMSE: 15.593 to 33.332 m (0.52 to 1.11 pixels)
Radiometric performance (offset, slope, R^2, uncertainty [%])	
Radiometric evaluation (linear regression—EnMAP versus OLI reflectance)	Band 1: −0.012 to 0.000, 0.947 to 1.016, 0.807 to 0.949, 2.60 to 8.60 Band 2: −0.006 to 0.004, 0.956 to 1.023, 0.810 to 0.951, 3.18 to 10.63 Band 3: 0.000 to 0.007, 0.976 to 1.031, 0.816 to 0.954, 4.08 to 12.87 Band 4: 0.005 to 0.011, 0.959 to 0.995, 0.821 to 0.956, 4.45 to 13.34 Band 5: −0.001 to 0.008, 0.978 to 1.007, 0.814 to 0.961, 4.40 to 10.48 Band 6: 0.012 to 0.020, 0.964 to 0.979, 0.848 to 0.968, 4.13 to 7.73 Band 7: 0.006 to 0.016, 0.960 to 0.989, 0.849 to 0.969, 4.13 to 8.57

Analysis

This section of the report describes the geometric and radiometric performance of the EnMAP hyperspectral sensor.

Geometric Performance

The geometric performance for the EnMAP sensor is characterized in terms of the band-to-band alignment and image-to-image relative geometric accuracy.

Band to Band

For this analysis, each band of the EnMAP imagery was registered against one reference band (band 31 at 572 nm). The relative differences are small, which indicates a high quality of band-to-band performance. The scene identifier used as an example image to compute band-to-band error is Mojave Desert and is shown in figure 1. Scene identifiers for all band-to-band scenes discussed in this report are provided in table 4.

The grid system and error vectors for band 20 are shown in figure 1 as an example using the Mojave Desert scene (table 4). The red arrow shows the relative error vector for each yellow grid, with x and y vector components representing the easting and northing error, respectively. Several grids with missing arrows represent the outliers.

The mean difference and root mean square error (RMSE) values for the easting direction are shown in figure 2, and those for the northing direction are shown in figure 3. Similarly, figures 4 and 5 are band-to-band results for the Permian Basin scene (table 4). The band-to-band results for the Salton Sea scene are shown in figures 6 and 7 (table 4). The band-to-band results of all three scenes are summarized in table 4, where the erroneous values near the water vapor bands were not included in summarizing a result range in table 4.

Image to Image

For this analysis, spectrally resampled EnMAP (ρ_i) was used, where the subscript i represents i-th OLI band. The spectral resampling of EnMAP hyperspectral reflectance $\rho_{EnMAP}(\lambda)$ is performed using Landsat OLI spectral response function, $\Re_{OLI\_i}(\lambda)$ (Barsi and others, 2014).

$$\rho_i = \frac{\int \rho_{EnMAP}(\lambda)\,\Re_{OLI\_i}(\lambda)d\lambda}{\int \Re_{OLI\_i}(\lambda)d\lambda}\,. \qquad (1)$$

Three scene pairs between EnMAP and OLI were used for image-to-image analysis. A normalized cross-correlation matrix was computed, and its local maxima were determined to estimate the mean error and root mean square error results shown in table 5 and represented in pixels at a 30-meter (m) GSD.

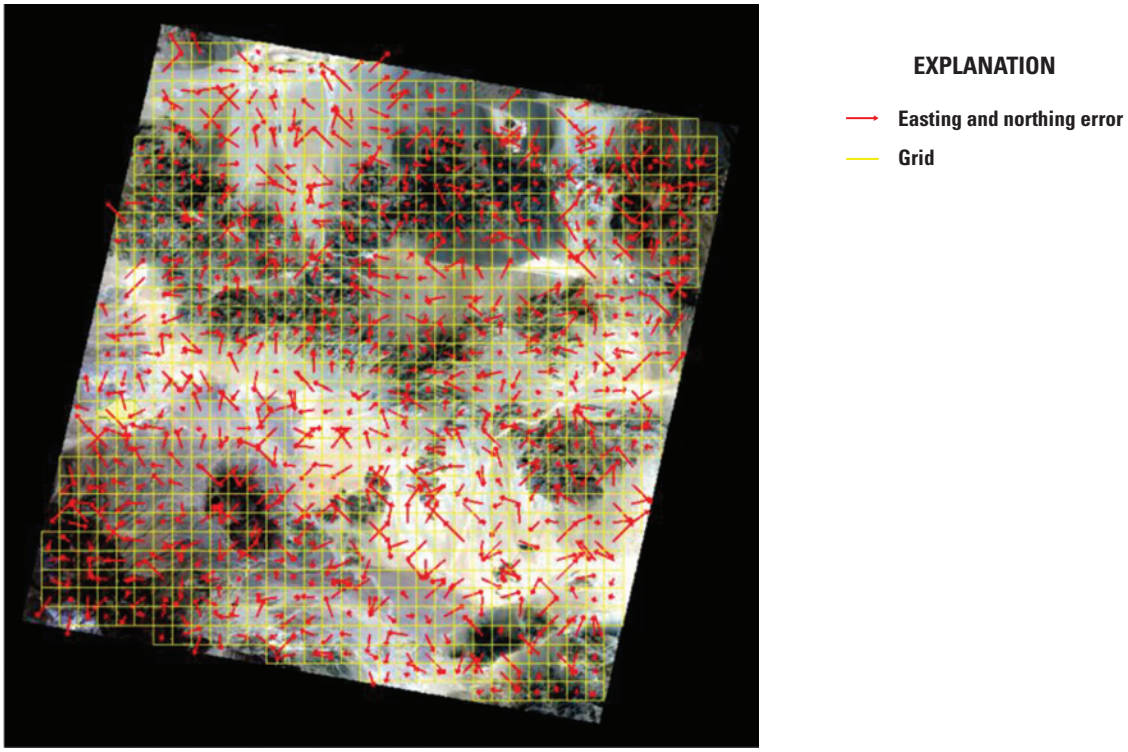

Figure 1. Image of grid showing band-to-band geometric error map of band 20 (516 nanometers) using band 31 (572 nanometers) as reference.

Table 4. Summary of band-to-band scene results using band 31 as a reference (in pixels).

[ID, identifier; RMSE, root mean square error]

Scene ID	Mean error (easting)	Mean error (northing)	RMSE (easting)	RMSE (northing)
Mojave Desert (ENMAP01-____L1C-DT 0000003185_20220905T191251Z_025_ V010401_20240222T085041Z)	−0.052 to 0.150	−0.103 to 0.012	0.204 to 0.451	0.197 to 0.419
Permian Basin (ENMAP01-____L1C-DT 0000014421_20230422T181254Z_013_ V010402_20240324T164154Z)	−0.043 to 0.137	−0.061 to 0.093	0.089 to 0.206	0.080 to 0.153
Salton Sea (ENMAP01-____L1C-DT 0000014115_20230424T190303Z_004_ V010402_20240324T172225Z)	−0.034 to 0.123	−0.135 to 0.019	0.124 to 0.315	0.119 to 0.313

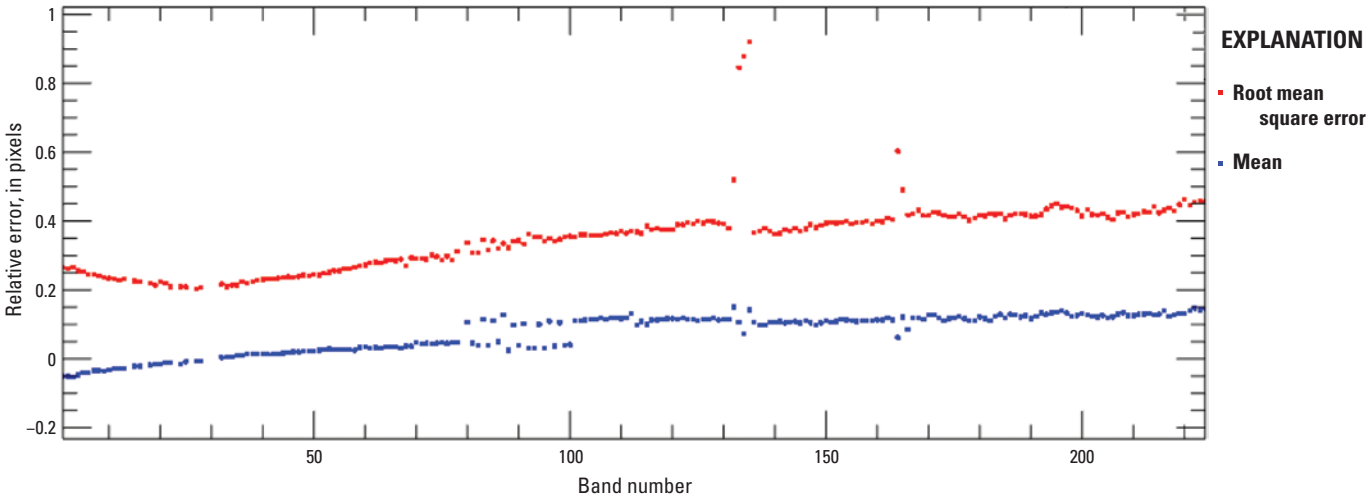

Figure 2. Graph showing the Mojave Desert scene band-to-band easting geometric error using band 31 as a reference.

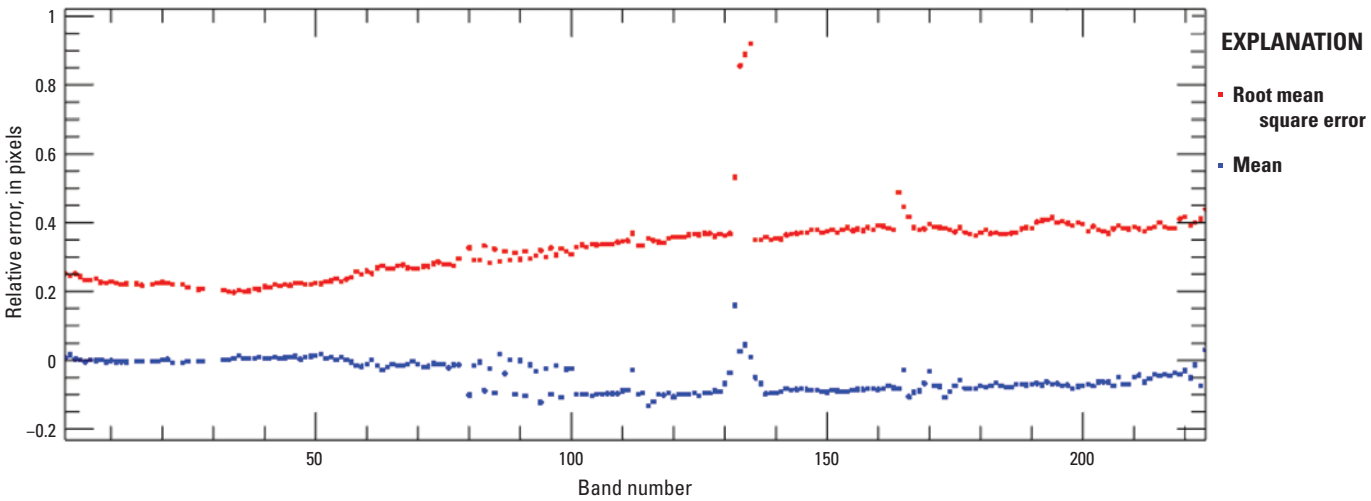

Figure 3. Graph showing the Mojave Desert scene band-to-band northing geometric error using band 31 as a reference.

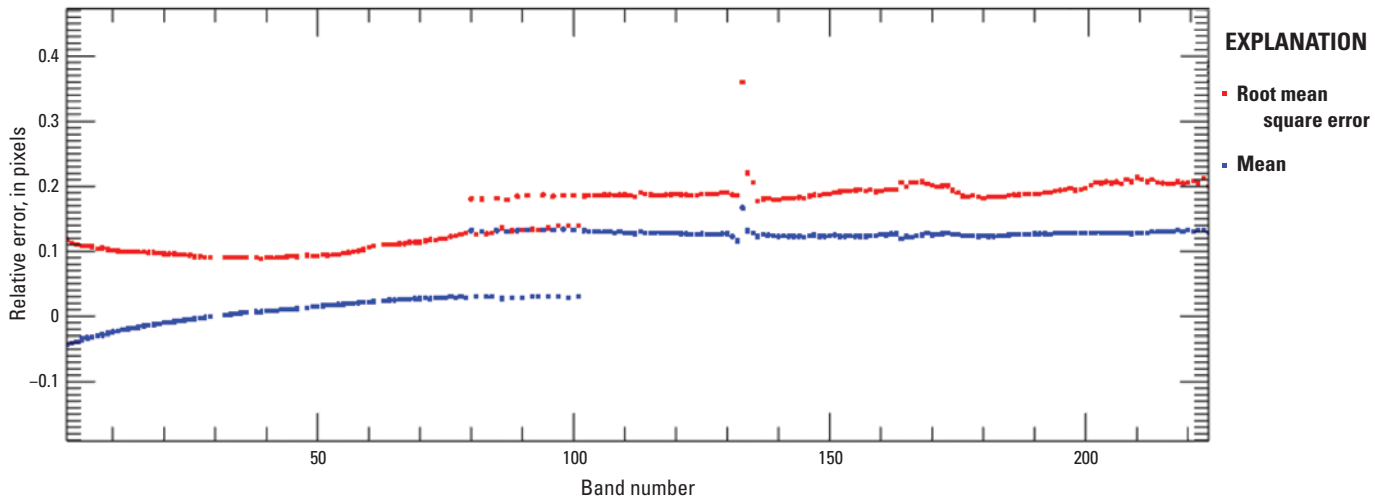

Figure 4. Graph showing the Permian Basin scene band-to-band easting geometric error using band 31 as a reference.

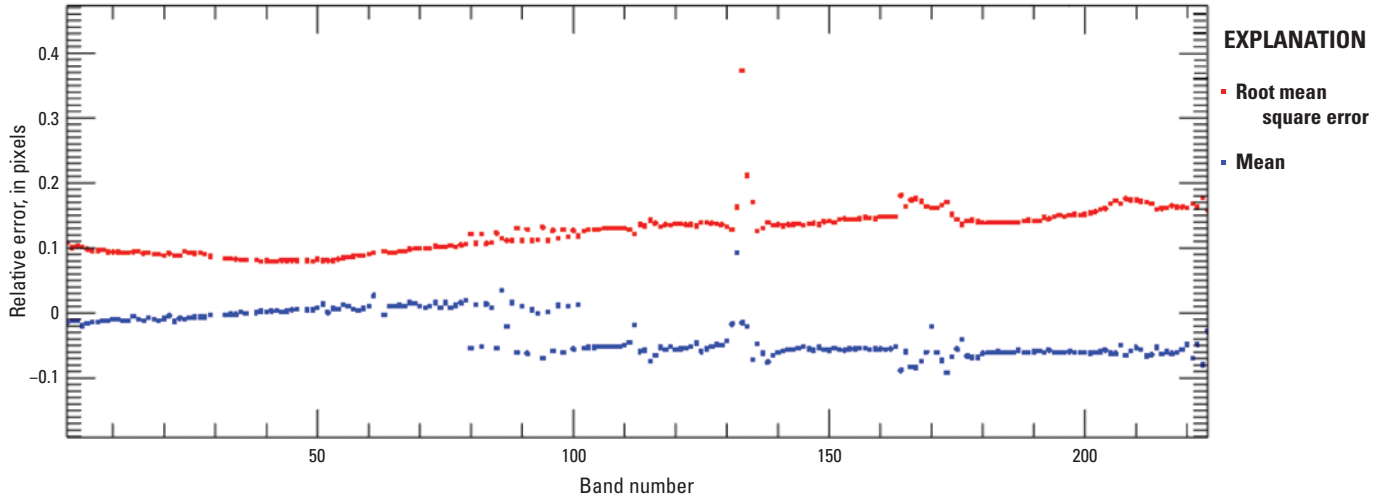

Figure 5. Graph showing the Permian Basin scene band-to-band northing geometric error using band 31 as a reference.

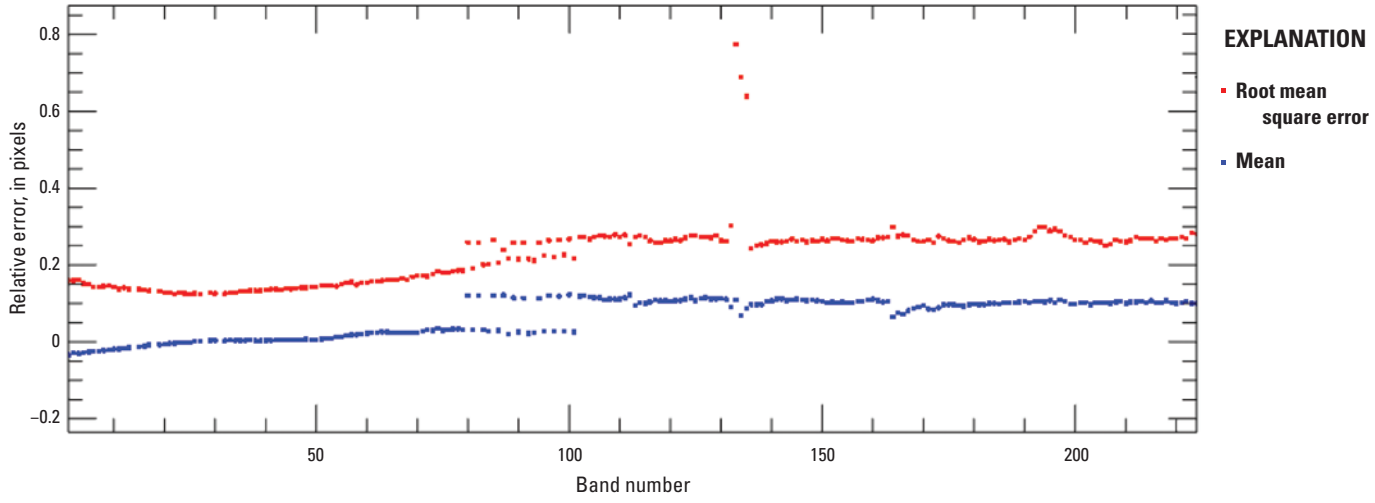

Figure 6. Graph showing the Salton Sea scene band-to-band easting geometric error using band 31 as a reference.

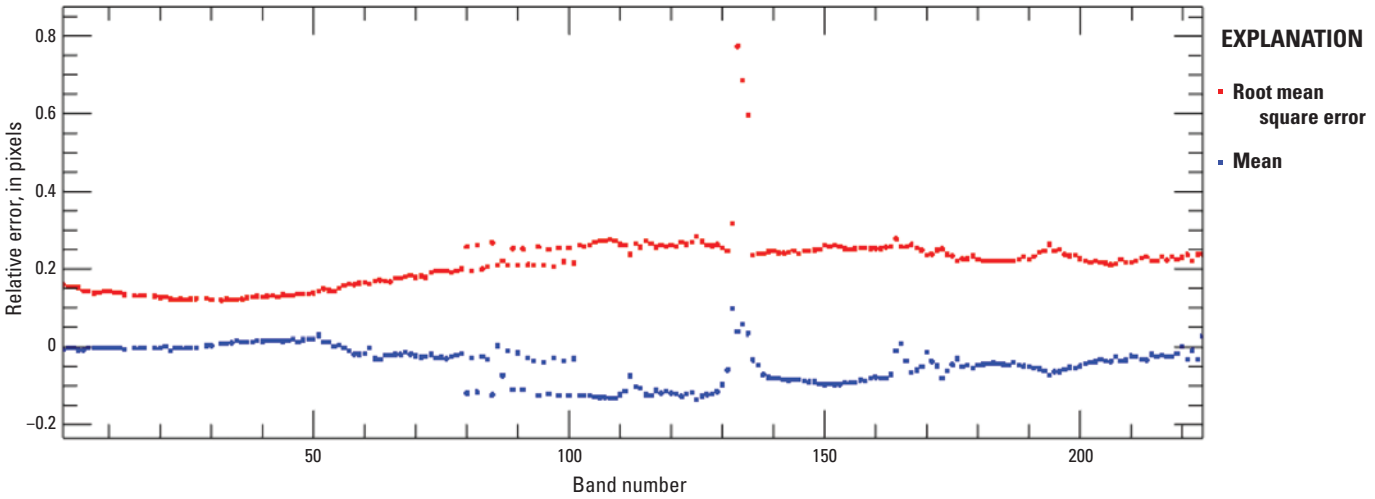

Figure 7. Graph showing Salton Sea scene visible and near infrared band-to-band northing geometric error using band 31 as a reference.

Table 5. Geometric error of the Environmental Mapping and Analysis Program relative to Landsat 8 Operational Land Imager imagery.

[ID, identifier; RMSE, root mean square error; m, meter]

Scene ID	Mean error (easting)	Mean error (northing)	RMSE (easting)	RMSE (northing)
Mojave Desert (ENMAP01-____L1C-DT 0000003185_20220905T191251Z_025_ V010401_20240222T085041Z) versus LC08_L1T P_040035_20220904_20220914_02_T1	−21.249 m (−0.71 pixel)	16.170 m (0.54 pixel)	22.352 m (0.75 pixel)	17.011 m (0.57 pixel)
Permian Basin (ENMAP01-____L1C-DT 0000014421_20230422T181254Z_013_ V010402_20240324T164154Z) versus LC09_L1T P_030038_20230418_20230418_02_T1	−27.716 m (−0.92 pixel)	32.892 m (1.09 pixels)	28.375 m (0.95 pixel)	33.332 m (1.11 pixels)
Salton Sea (ENMAP01-____L1C-DT 0000014115_20230424T190303Z_004_ V010402_20240324T172225Z) versus LC08_L1T P_039037_20230425_20230501_02_T1	−18.892 m (−0.63 pixel)	15.307 m (0.51 pixel)	19.517 m (0.65 pixel)	15.593 m (0.52 pixel)

For each of the three EnMAP images, geometric error maps illustrating the directional shift and relative magnitude of the shift, when compared with Landsat 8 OLI, are provided in figures 8 through 16.

Radiometric Performance

For this analysis, cloud-free regions of interest were selected within three near-coincident EnMAP and Landsat 8 OLI scene pairs. Top of Atmosphere reflectance (TOAR) comparison results are listed in table 6.

Once the relative georeferencing error between the Landsat 8 OLI and EnMAP has been corrected, TOAR values from the two sensors are extracted. The scatter plots shown in figures 17 through 19 are drawn in a way that the x-axis is the reference sensor (Landsat OLI) and the y-axis is the comparison sensor (EnMAP). Ideally, the slope should be near unity (1.0) and the offset should be near zero, and if the slope is greater than unity, that means EnMAP tends to overestimate TOAR compared to Landsat 8 OLI. A band-by-band graphical comparison of the Mojave Desert, Permian Basin, and Salton Sea scene image pair is shown in figures 17, 18, and 19, respectively.

Comparison to Radiometric Calibration Network

The EnMAP hyperspectral data were cross-checked against Radiometric Calibration Network (RadCalNet) data. The EnMAP image used for the one comparison was at the

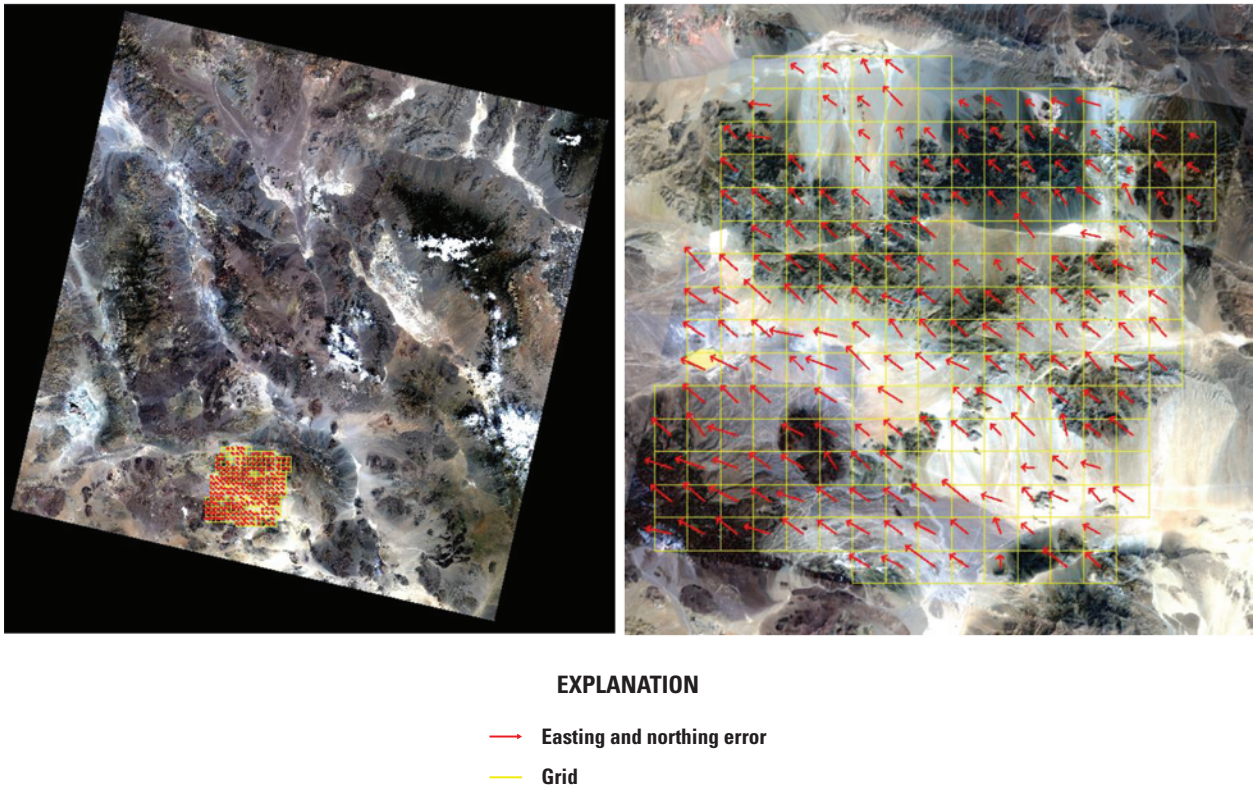

Figure 8. Image-to-image geometric error map using the Mojave Desert scene image pair.

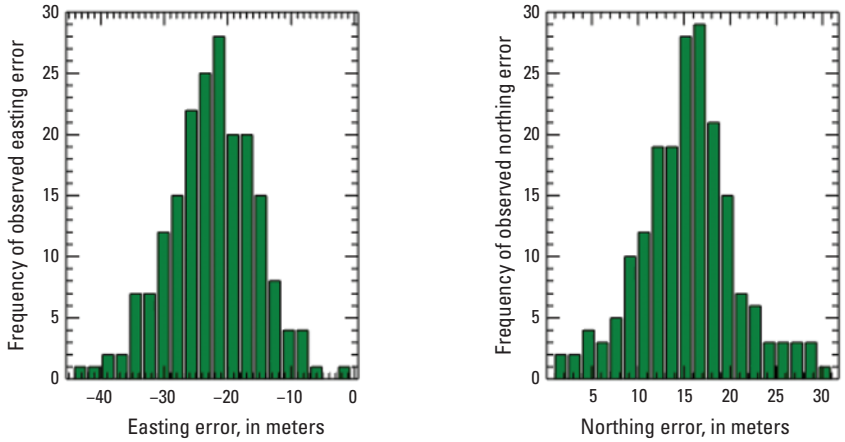

Figure 9. Histogram of image-to-image geometric error using the Mojave Desert scene image pair.

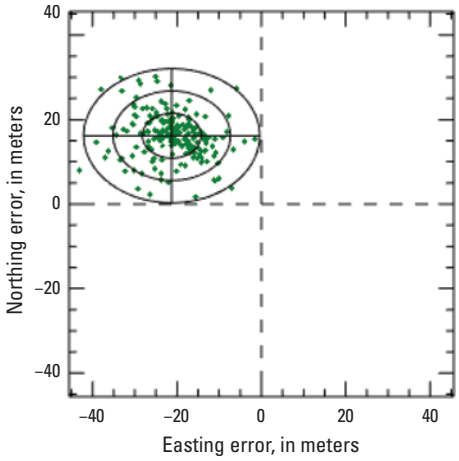

Figure 10. Error scatter plot of image-to-image geometric error using the Mojave Desert scene image pair.

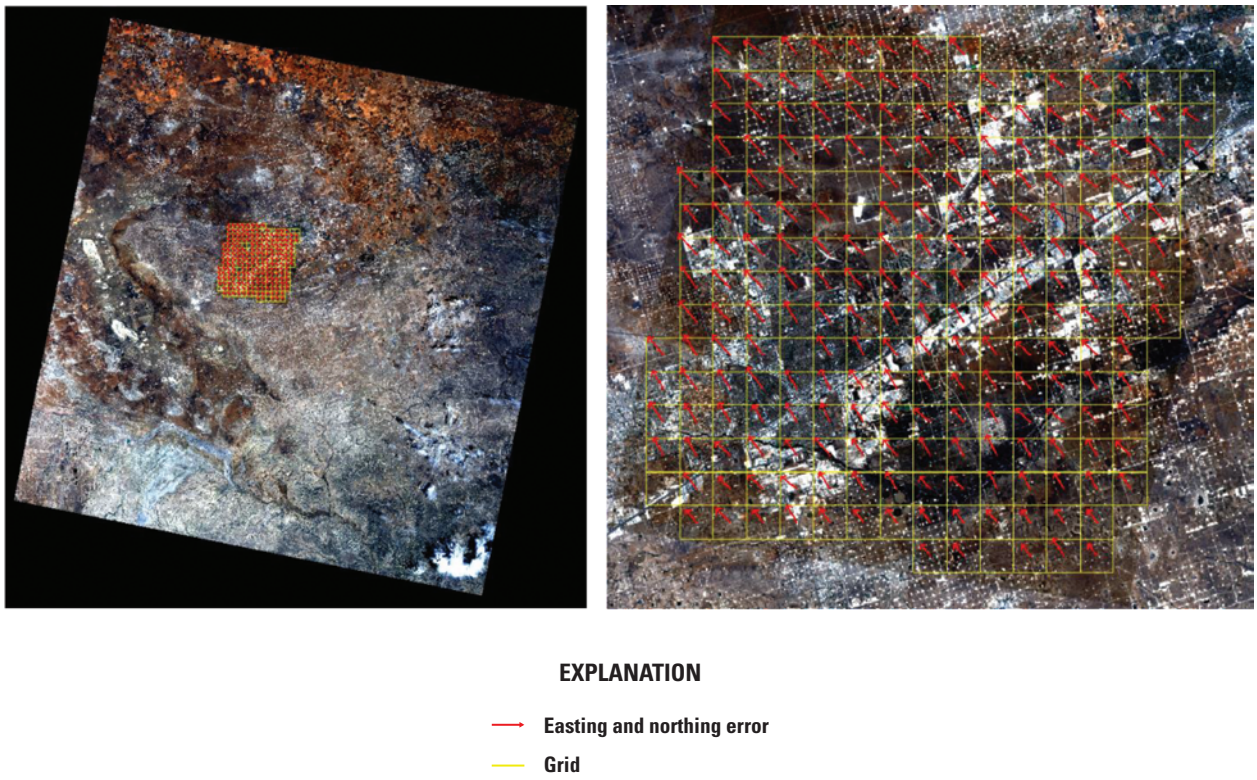

Figure 11. Image-to-image geometric error map using the Permian Basin scene image pair.

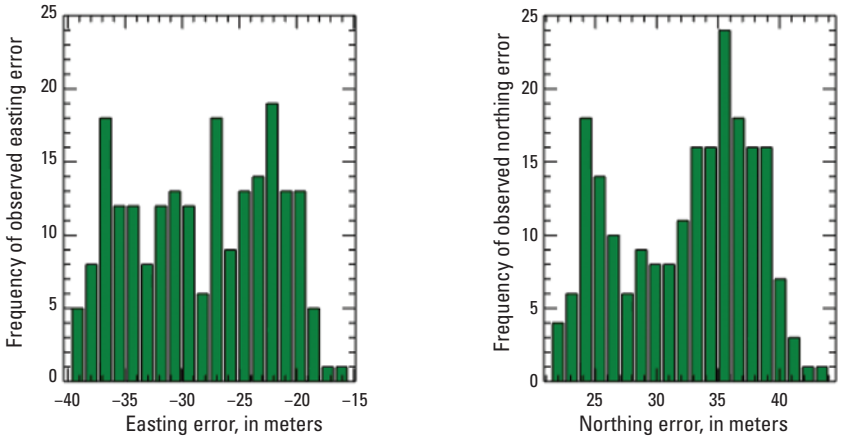

Figure 12. Histogram of image-to-image geometric error using the Permian Basin scene image pair.

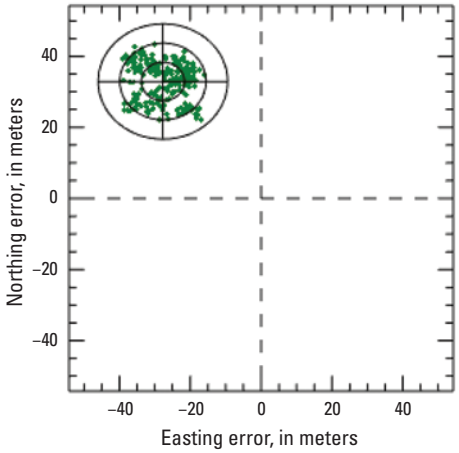

Figure 13. Error scatter plot of image-to-image geometric error using the Permian Basin scene image pair.

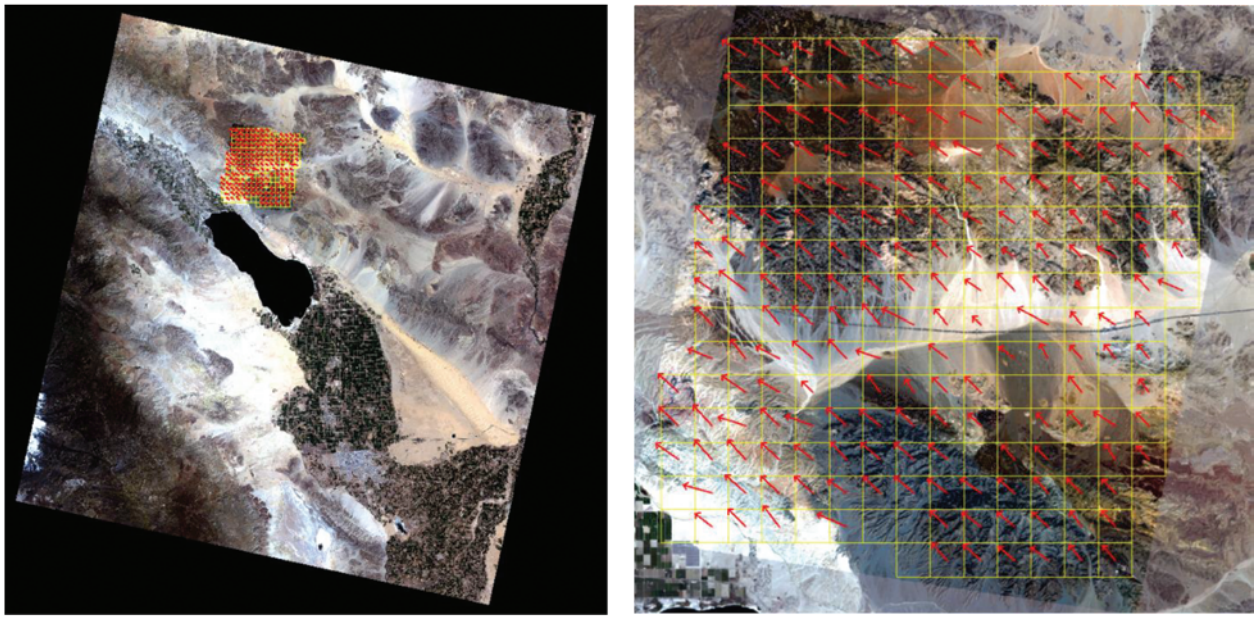

Figure 14. Image-to-image geometric error map using Salton Sea scene image pair.

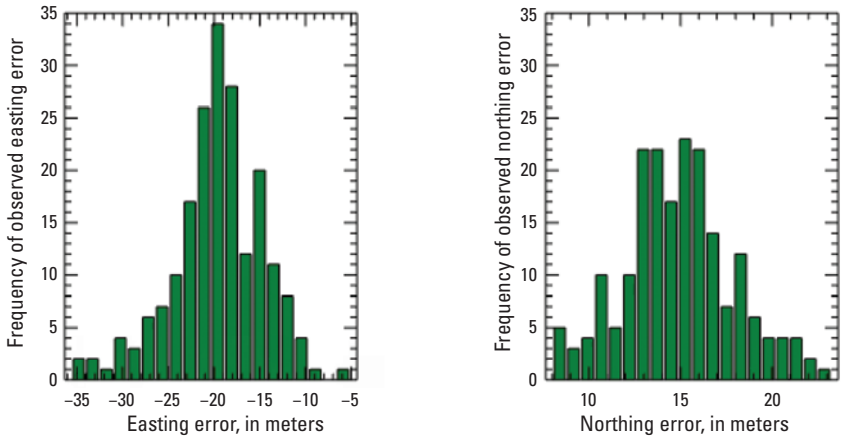

Figure 15. Histogram of image-to-image geometric error using Salton Sea scene image pair.

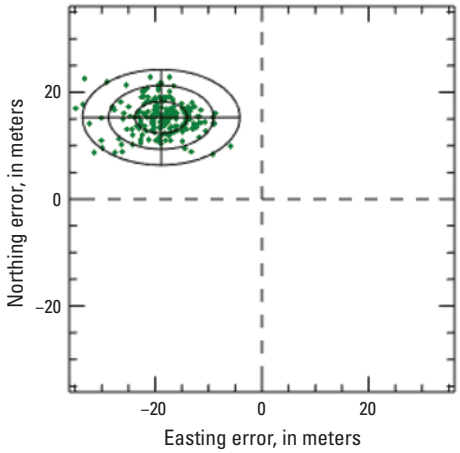

Figure 16. Error scatter plot of image-to-image geometric error using Salton Sea scene image pair.

Table 6. Top of Atmosphere reflectance comparison for the Environmental Mapping and Analysis Program against Landsat 8 Operational Land Imager (OLI).

[ID, identifier; B, band; CA, coastal aerosol; NIR, near infrared; SW, shortwave infrared; %, percent; R^2, coefficient of determination]

Scene IDs	Statistics	B1 (CA)	B2 (blue)	B3 (green)	B4 (red)	B5 (NIR)	B6 (SW1)	B7 (SW2)
Mojave Desert (ENMAP01-____L1C-DT0000003185_20220905T191251Z_025_V010401_20240222T085041Z) versus LC08_L1TP_040035_20220904_20220914_02_T1	Uncertainty (%)	2.60	3.18	4.08	4.45	4.40	4.13	4.13
	R^2	0.949	0.951	0.954	0.956	0.961	0.968	0.969
	Regression offset	0.000	0.004	0.007	0.010	−0.001	0.012	0.009
	Regression slope	0.947	0.956	0.976	0.959	0.981	0.964	0.970
Permian Basin (ENMAP01-____L1C-DT0000014421_20230422T181254Z_013_V010402_20240324T164154Z) versus LC09_L1TP_030038_20230418_20230418_02_T1	Uncertainty (%)	8.60	10.63	12.87	13.34	10.48	7.73	8.57
	R^2	0.807	0.810	0.816	0.821	0.814	0.848	0.849
	Regression offset	−0.012	−0.006	0.000	0.005	0.008	0.012	0.006
	Regression slope	1.016	1.023	1.031	0.995	0.978	0.979	0.989
Salton Sea (ENMAP01-____L1C-DT0000014115_20230424T190303Z_004_V010402_20240324T172225Z) versus LC08_L1TP_039037_20230425_20230501_02_T1	Uncertainty (%)	2.90	3.700	5.10	5.59	5.57	5.40	5.52
	R^2	0.936	0.931	0.922	0.915	0.926	0.934	0.936
	Regression offset	−0.004	0.001	0.005	0.011	0.005	0.020	0.016
	Regression slope	1.006	1.010	1.025	0.989	1.007	0.975	0.960

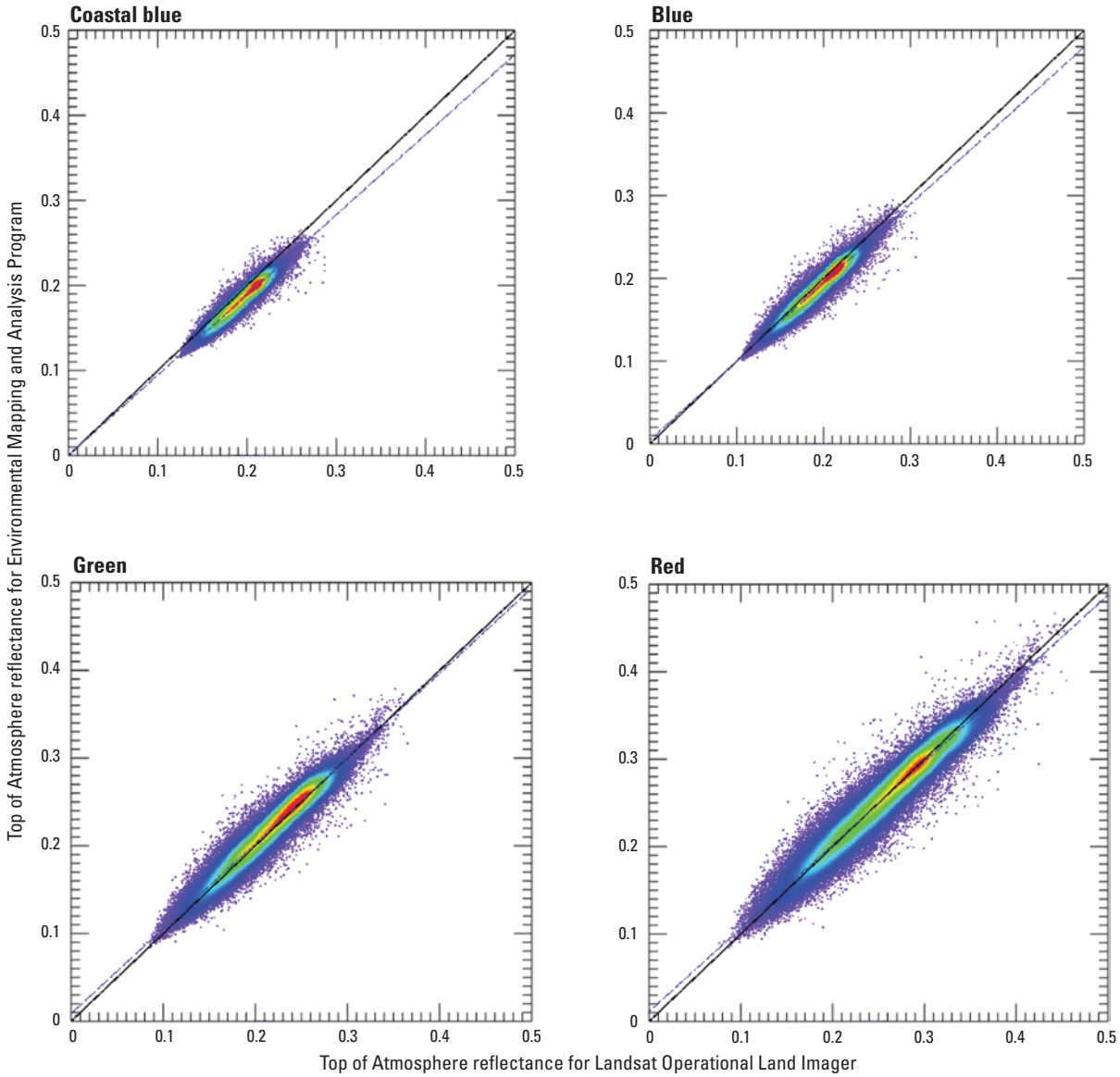

Figure 17. Radiometric scatter plot using the Mojave Desert scene image pair.

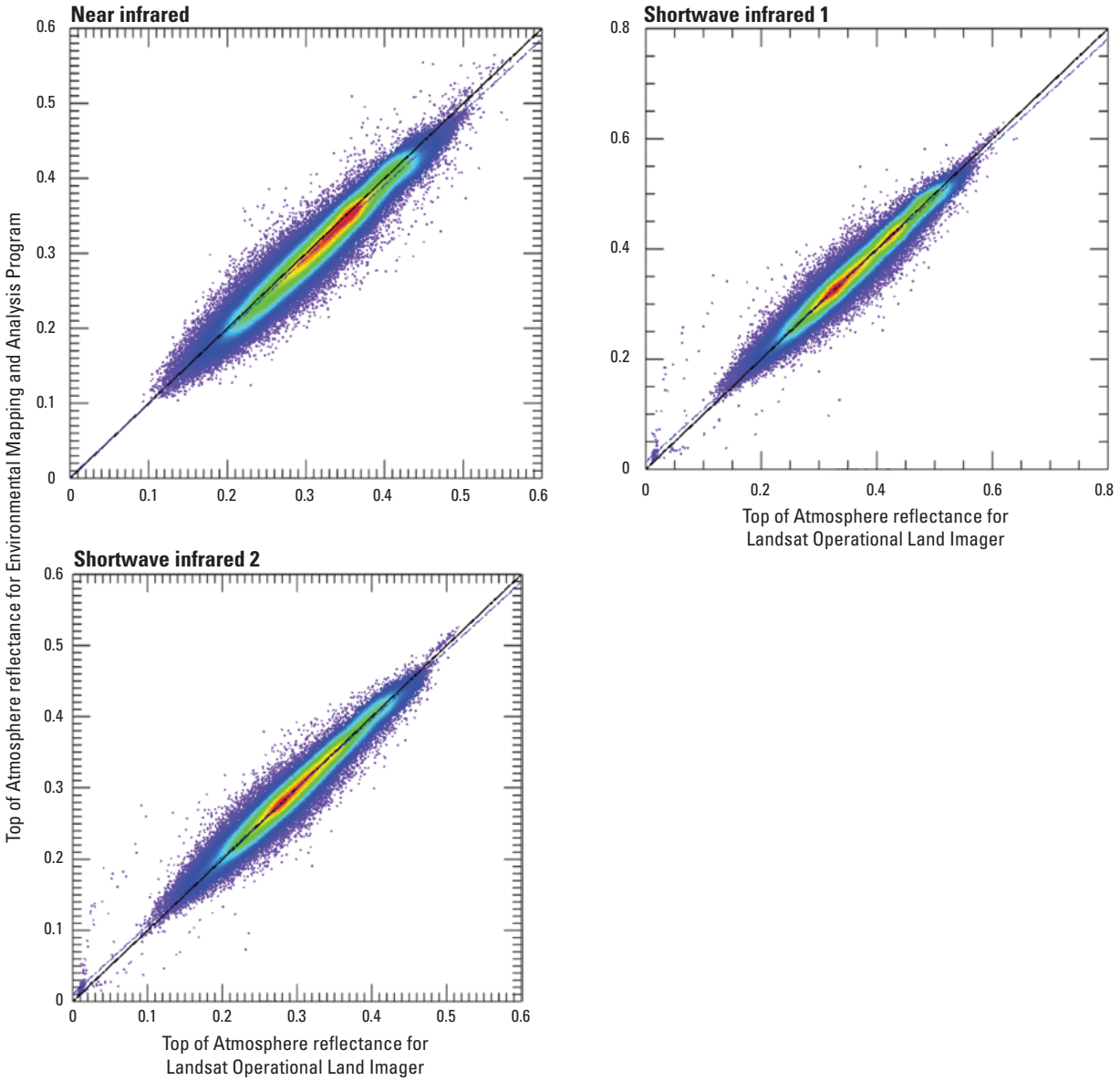

Figure 17. Radiometric scatter plot using the Mojave Desert scene image pair.—Continued

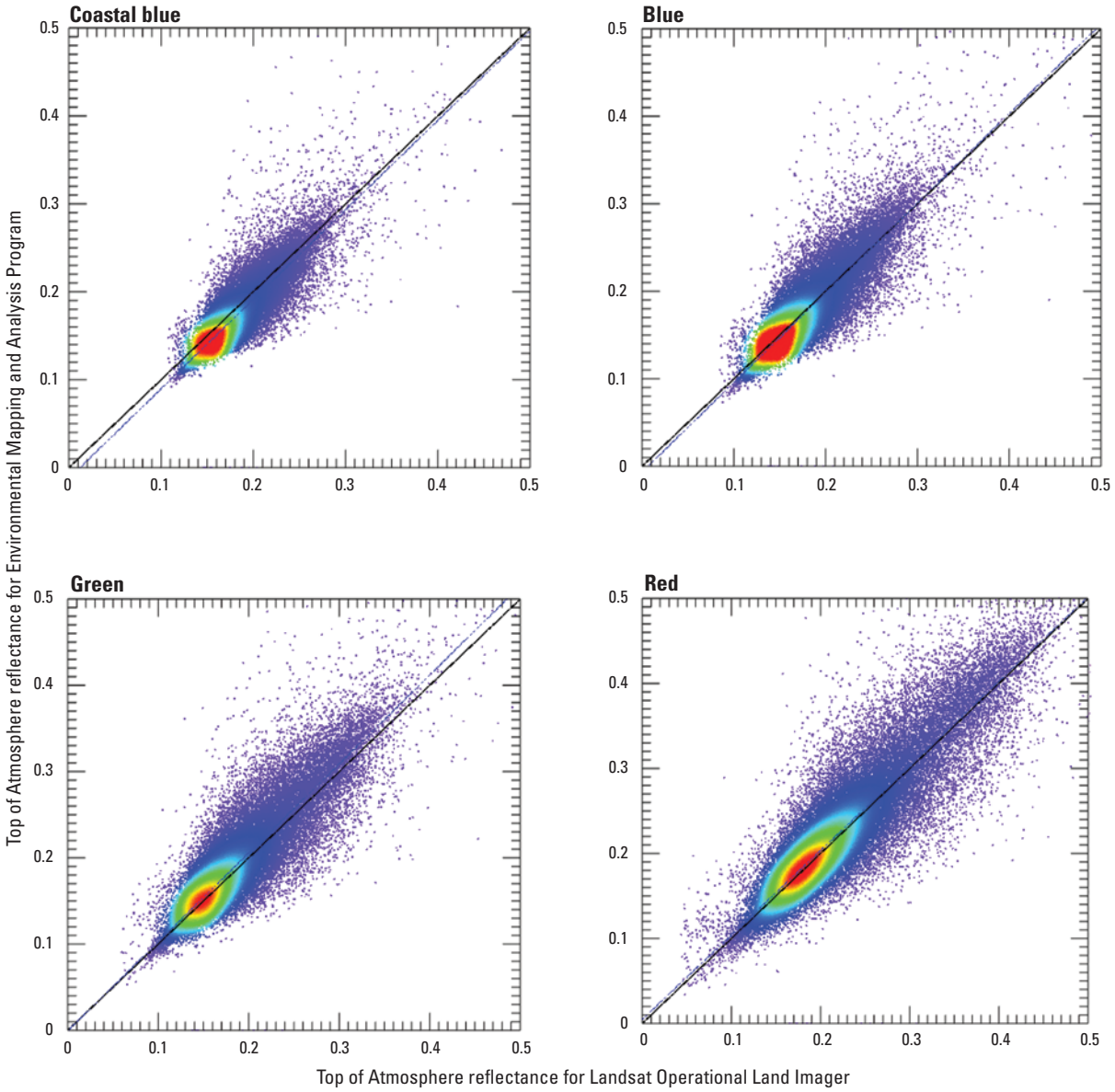

Figure 18. Radiometric scatter plot using the Permian Basin scene image pair.

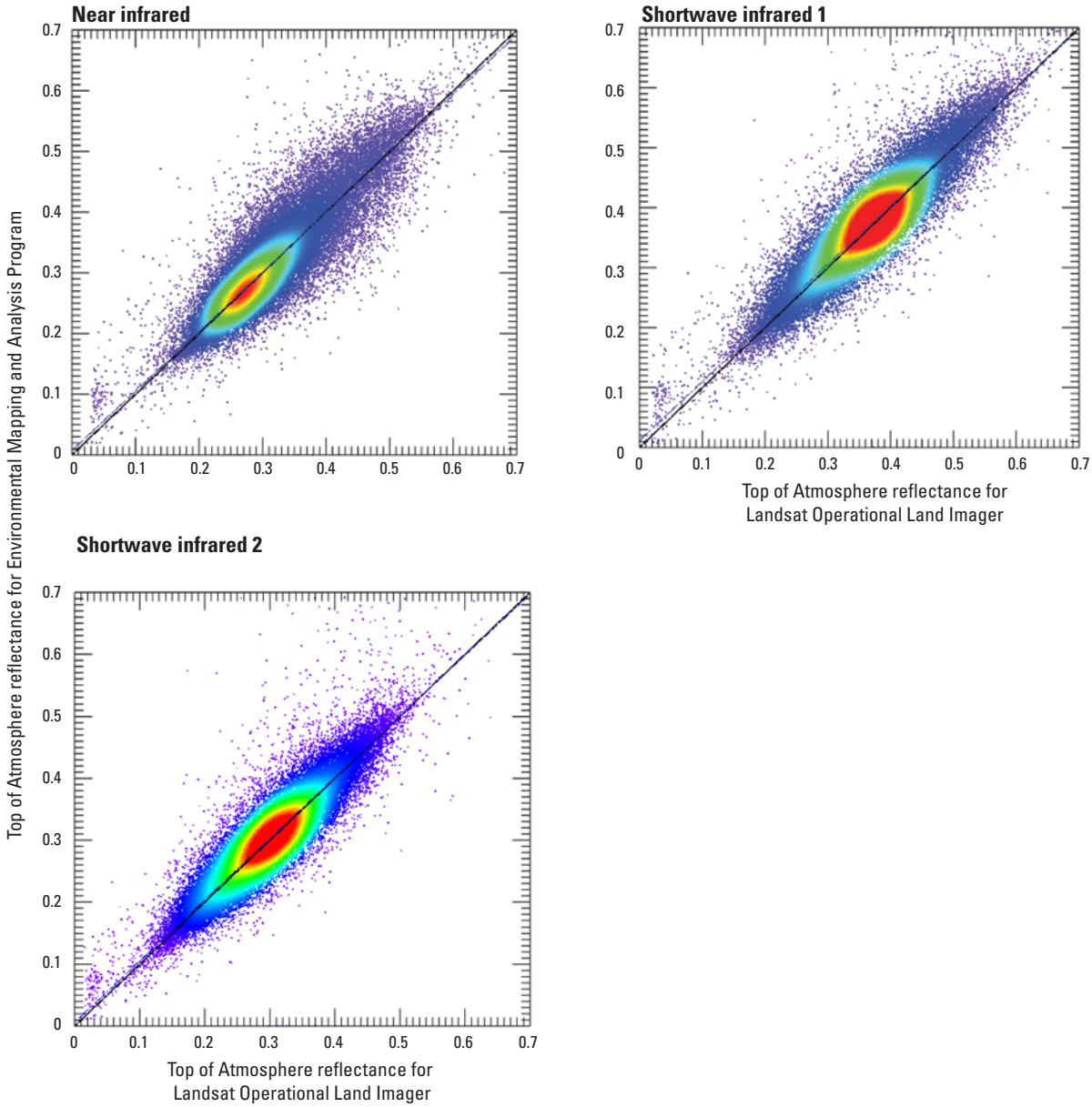

Figure 18. Radiometric scatter plot using the Permian Basin scene image pair.—Continued

Gobabeb, Namibia, scene (ENMAP01-____L1C-DT0000002809_20220825T095656Z_003_V010301_20230512T042908Z). The RadCalNet data were not available on the date (August 25, 2023), but the day before (August 24, 2023) and after (August 26, 2023) were available. Based on the inspection, the differences between the two datasets were negligible, so the average of the two datasets (GONA01_2022_236_v00.08.input; GONA01_2022_238_v00.08.input) was used for the comparison. The reflectance between EnMAP and RadCalNet at the Gobabeb, Namibia, scene is compared in figure 20.

RadCalNet measured the surface reflectance (SR; magenta curve) and then estimated satellite TOAR (yellow curve) using atmospheric measurements. Conversely, EnMAP measured TOAR (white curve, L1 product) from the satellite and then estimated SR (cyan curve, L2 product) by atmospheric correction. Also shown in figure 20 is the image of the GONA RadCalNet site.

The comparison between the two hyperspectral data (either two TOAR curves or two SR curves) is indicated by the plots in figure 20, but a quantitative measure was not attempted. There are many statistical indices to compare the two vectors. For hyperspectral data, it is customary to use spectral angle measurements to describe the similarity

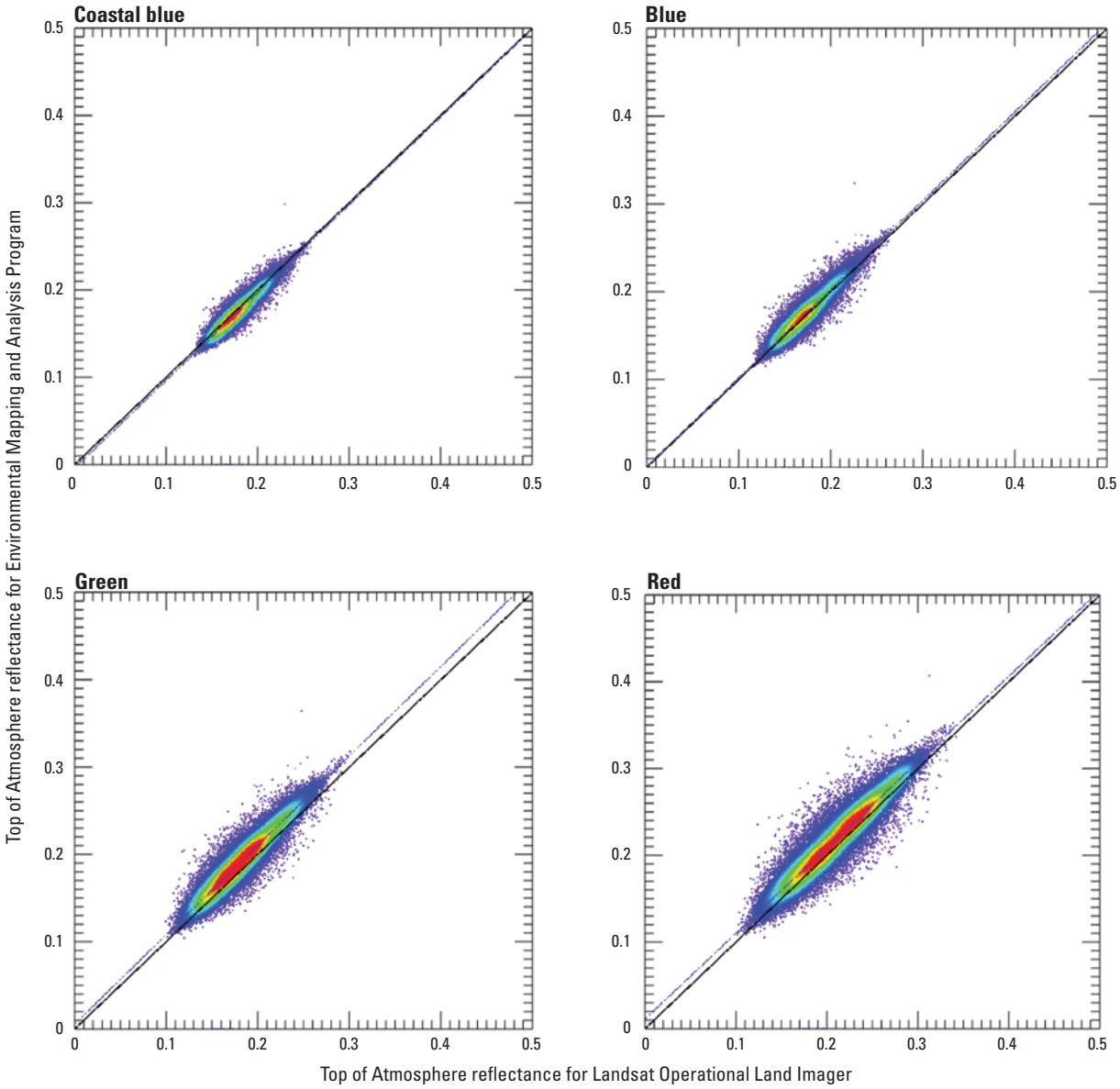

Figure 19. Radiometric scatter plot using the Salton Sea scene image pair.

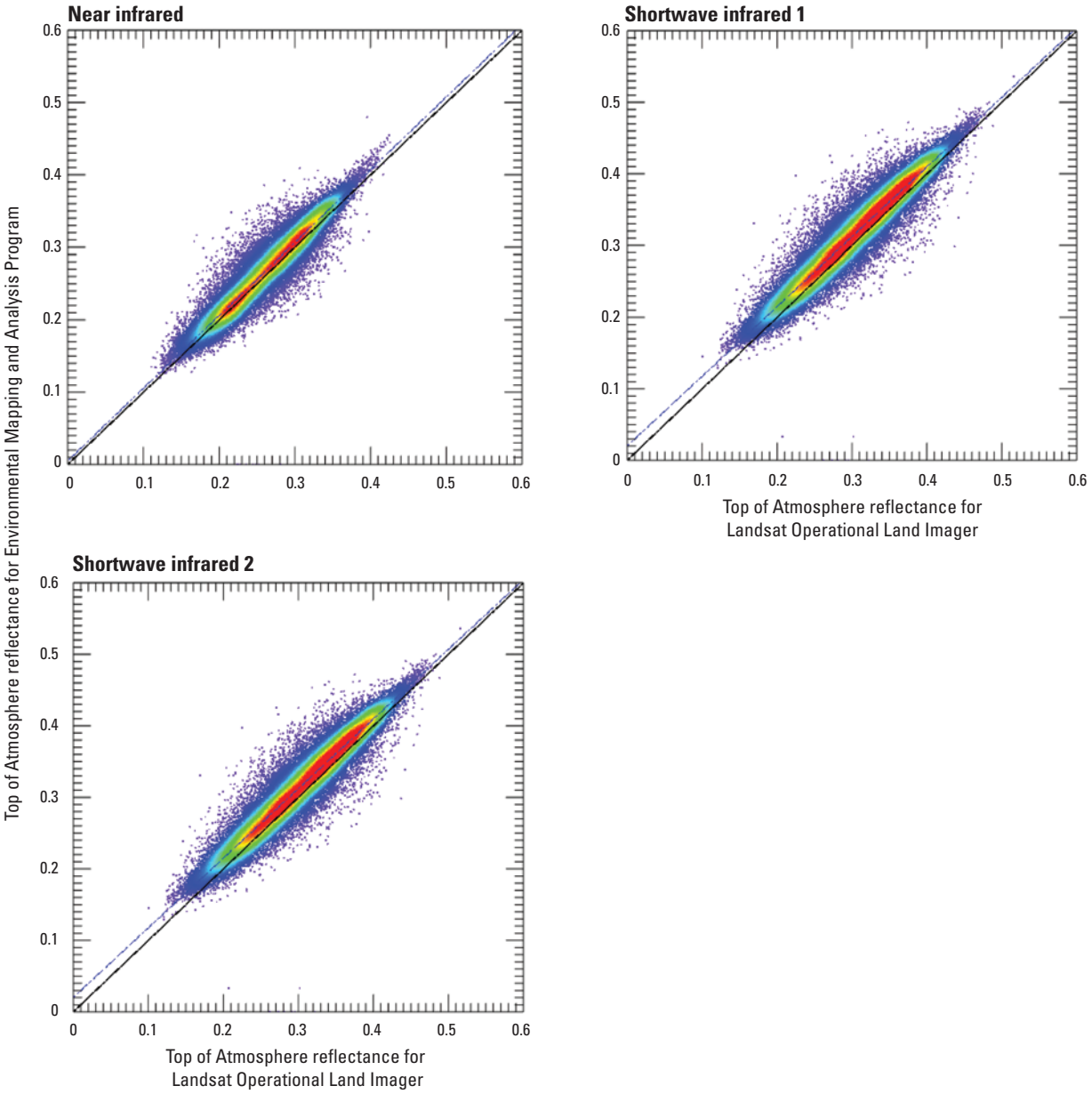

Figure 19. Radiometric scatter plot using the Salton Sea scene image pair.—Continued

between the two spectra; however, for remotely sensed data that include many water vapor absorption bands, the vast differences in the water vapor bands will completely dominate any quantitative measurements in a substantially negative way. Thus, the measurement is subjective and highly dependent on band selection; therefore, instead of providing a questionable quantitative measurement in the report, the user is encouraged to visually evaluate the spectral differences.

The EnMAP image used for the comparison was at the La Crau, France, scene (ENMAP01-____L1C-DT0000001252_20220628T111310Z_032_V010301_20230512T044237Z). The closest RadCalNet data available were 4 days apart on July 2, 2022 (LCFR01_2022_183_v00.04.input). The reflectance between EnMAP and RadCalNet at LFCR is compared in figure 21. RadCalNet measured the SR (magenta curve) and then estimated satellite TOAR (yellow curve) based on atmospheric measurements. Conversely, EnMAP measured TOAR (white curve, L1 product) from the satellite and then estimated SR (cyan curve, L2 product) by atmospheric correction. Also shown in figure 21 is the image of the La Crau, France, RadCalNet site.

The EnMAP image was also used for the comparison at the Railroad Valley Playa, United States, scene (ENMAP01-____L1C-DT0000004447_20221014T192304Z_005_V010301_20230512T044441Z). The closest RadCalNet data available were 1 day apart on October 15,

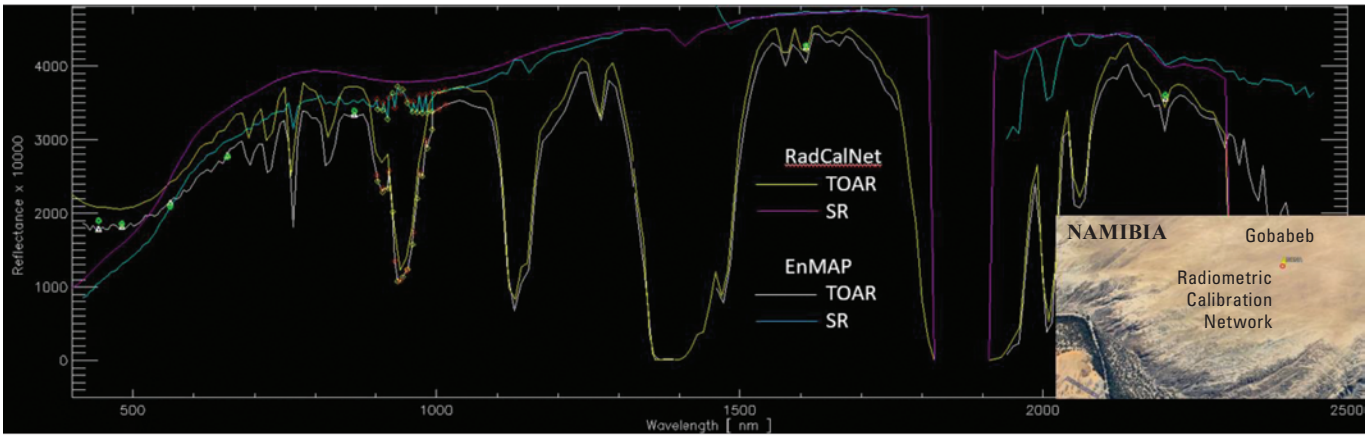

EXPLANATION

RadCalNet	Radiometric Calibration Network
TOAR	Top of Atmosphere reflectance
SR	Surface reflectance
EnMAP	Environmental Mapping and Analysis Program
nm	Nanometer

Figure 20. Graph showing comparison of reflectance between the Environmental Mapping and Analysis Program (EnMAP) and the Radiometric Calibration Network (RadCalNet) at Gobabeb, Namibia.

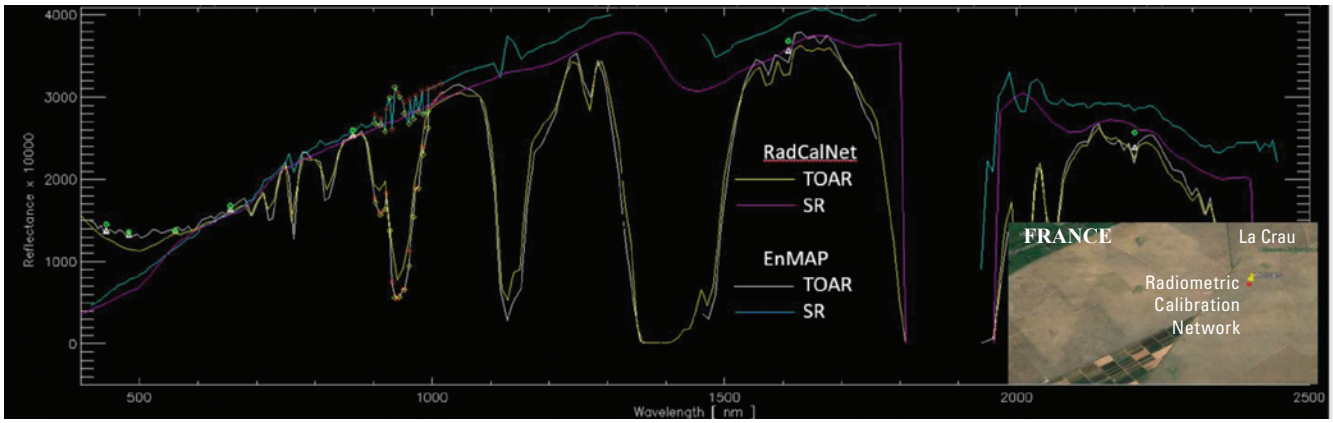

EXPLANATION

RadCalNet	Radiometric Calibration Network
TOAR	Top of Atmosphere reflectance
SR	Surface reflectance
EnMAP	Environmental Mapping and Analysis Program
nm	Nanometer

Figure 21. Graph showing comparison of reflectance between the Environmental Mapping and Analysis Program (EnMAP) and the Radiometric Calibration Network (RadCalNet) at La Crau, France.

2022 (RVUS00_2022_288_v00.05.input). The reflectance between EnMAP and RadCalNet at Railroad Valley Playa, United States, is compared in figure 22. RadCalNet measured the SR (magenta curve) and then estimated satellite TOAR (yellow curve) using atmospheric measurements. Conversely, EnMAP measured TOAR (white curve, L1 product) from the satellite and then estimated SR (cyan curve, L2 product) by atmospheric correction. Also shown in figure 22 is the image of the Railroad Valley Playa, United States, RadCalNet site.

Comparison of Hyperspectral and In Situ Reflectance Spectrometer Data

The EnMAP hyperspectral data were cross-checked against in situ hyperspectral data measured using ASD FieldSpec spectrometer by Malvern Panalytical (hereafter referred to as "spectrometer data"). The EnMAP image used for the comparison was at the USGS Earth Resources Observation and Science Center (ENMAP01-____L1C-DT0000001649_20220714T175823Z_002_V010301_20230523T071525Z). The location of the USGS Earth Resources Observation and Science Center in situ data collection site is shown in figure 23 and indicated by the red box in the photograph.

The reflectance between EnMAP and the spectrometer data is shown in figure 24.

The spectrometer was used to measure the SR (magenta curve) on July 14, 2022. Conversely, EnMAP measured TOAR (white curve, L1 product) from the satellite and then estimated SR (cyan curve, L2 product) by atmospheric correction, thus, the comparison between the two SR curves (magenta and cyan). The reflectance between the EnMAP and the spectrometer data on July 18, 2022, is compared in figure 25 (ENMAP01-____L1C-DT0000001723_20220718T180157Z_002_V010301_20230523T071522Z).

The reflectance between the EnMAP and the spectrometer data on August 10, 2022, is compared in figure 26 (ENMAP01-____L1C-DT0000002409_20220810T175757Z_001_V010301_20230523T071516Z).

The reflectance between the EnMAP and the spectrometer data on September 2, 2022, is compared in figure 27 (ENMAP01-____L1C-DT0000003170_20220902T175434Z_002_V010301_20230523T071508Z).

The reflectance between the EnMAP and the spectrometer data on September 29, 2022, is compared in figure 28 (ENMAP01-____L1C-DT0000003953_20220929T175459Z_002_V010301_20230523T071437Z).

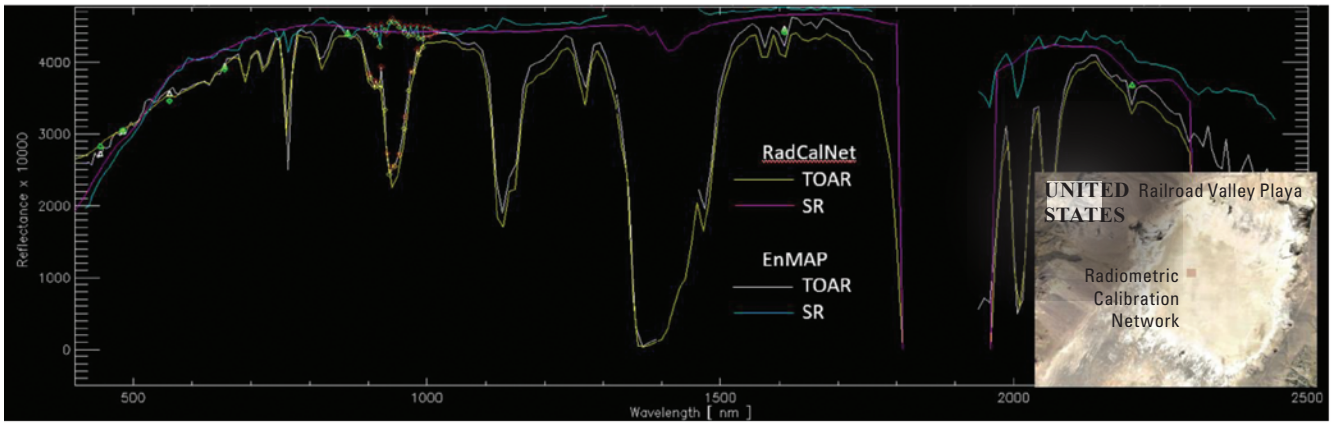

EXPLANATION

RadCalNet	Radiometric Calibration Network
TOAR	Top of Atmosphere reflectance
SR	Surface reflectance
EnMAP	Environmental Mapping and Analysis Program
nm	Nanometer

Figure 22. Graph showing comparison of reflectance between the Environmental Mapping and Analysis Program (EnMAP) and the Radiometric Calibration Network (RadCalNet) at Railroad Valley Playa, United States (RVUS).

Figure 23. Image showing the location (red box) of the spectrometer measurements at the U.S. Geological Survey Earth Resources Observation and Science Center (USGS EROS). The background scene identifier of an Operational Land Imager image is LC09_L1TP_029030_20220830_20230331_02_T1.

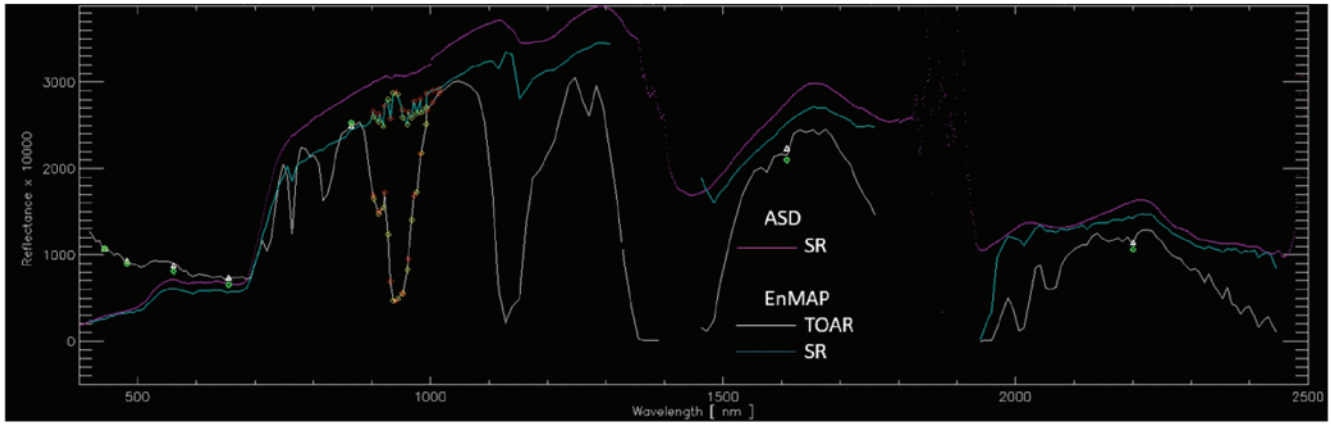

EXPLANATION

ASD	**Analytical Spectral Devices**
SR	**Surface reflectance**
EnMAP	**Environmental Mapping and Analysis Program**
TOAR	**Top of Atmosphere reflectance**
nm	**Nanometer**

Figure 24. Graph showing comparison of reflectance between the Environmental Mapping and Analysis Program (EnMAP) and the spectrometer data at the U.S. Geological Survey Earth Resources Observation and Science Center on July 14, 2022.

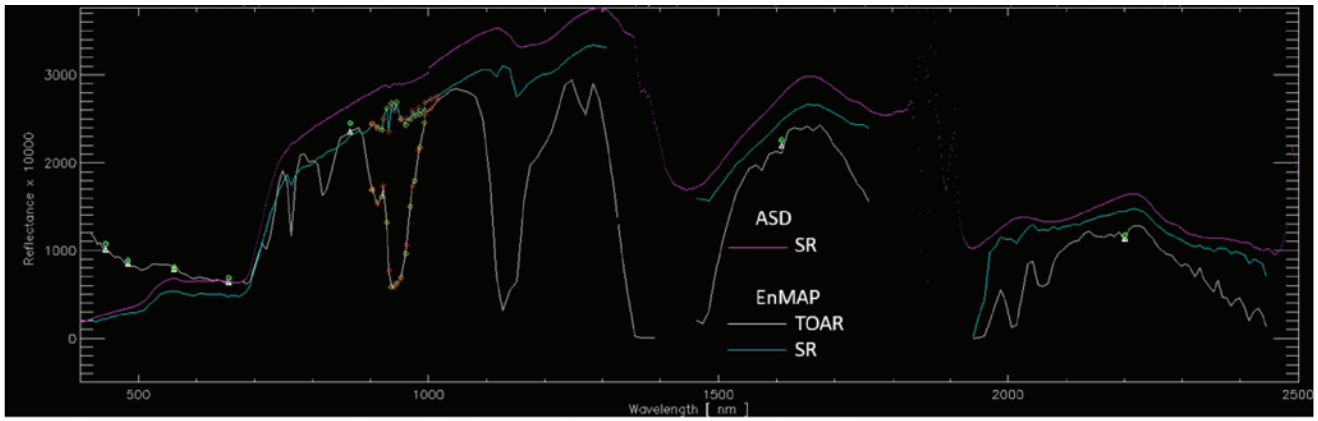

EXPLANATION

ASD	**Analytical Spectral Devices**
SR	**Surface reflectance**
EnMAP	**Environmental Mapping and Analysis Program**
TOAR	**Top of Atmosphere reflectance**
nm	**Nanometer**

Figure 25. Graph showing comparison of reflectance between the Environmental Mapping and Analysis Program (EnMAP) and the spectrometer data at the U.S. Geological Survey Earth Resources Observation and Science Center on July 18, 2022.

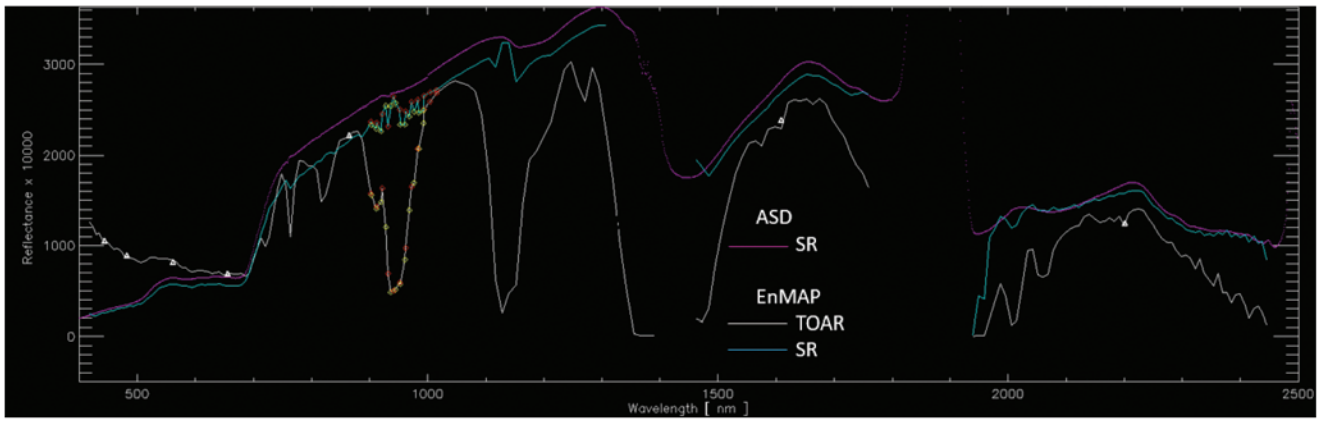

EXPLANATION

ASD	**Analytical Spectral Devices**
SR	**Surface reflectance**
EnMAP	**Environmental Mapping and Analysis Program**
TOAR	**Top of Atmosphere reflectance**
nm	**Nanometer**

Figure 26. Graph showing comparison of reflectance between the Environmental Mapping and Analysis Program (EnMAP) and the spectrometer data at the U.S. Geological Survey Earth Resources Observation and Science Center on August 10, 2022.

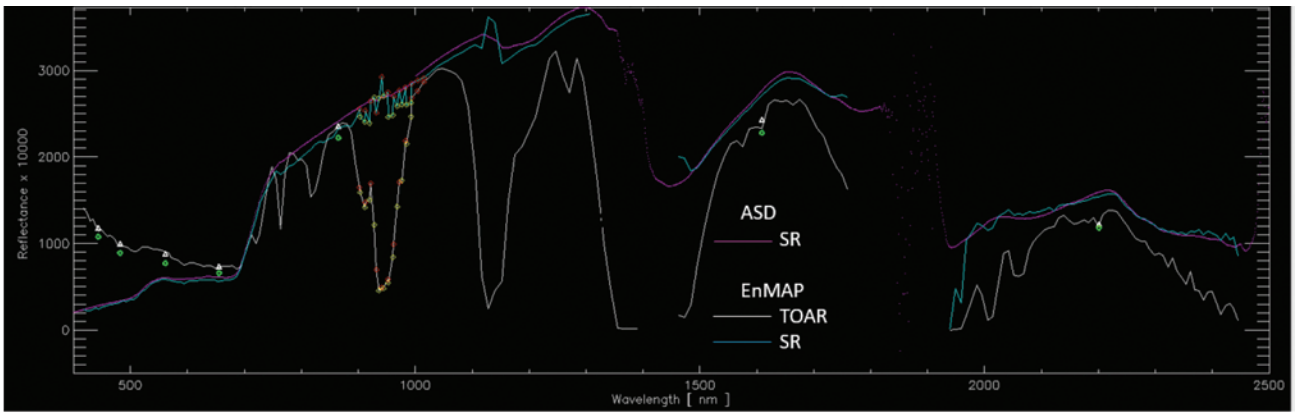

EXPLANATION

ASD	**Analytical Spectral Devices**
SR	**Surface reflectance**
EnMAP	**Environmental Mapping and Analysis Program**
TOAR	**Top of Atmosphere reflectance**
nm	**Nanometer**

Figure 27. Graph showing comparison of reflectance between the Environmental Mapping and Analysis Program (EnMAP) and the spectrometer data at the U.S. Geological Survey Earth Resources Observation and Science Center on September 2, 2022.

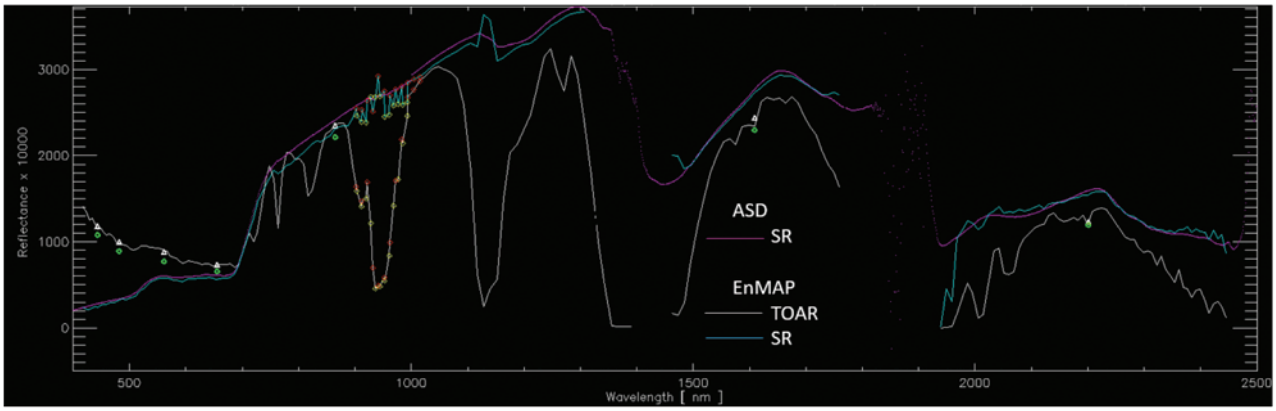

EXPLANATION

ASD	**Analytical Spectral Devices**
SR	**Surface reflectance**
EnMAP	**Environmental Mapping and Analysis Program**
TOAR	**Top of Atmosphere reflectance**
nm	**Nanometer**

Figure 28. Graph showing comparison of reflectance between the Environmental Mapping and Analysis Program (EnMAP) and the spectrometer data at the U.S. Geological Survey Earth Resources Observation and Science Center on September 29, 2022.

Discussion on Intersensor Georeferencing Error

The two sensors (visible and near infrared [VNIR] and shortwave infrared [SWIR]) share the same telescope. However, the field splitter slit assembly diverges the incident light to each sensor (Guanter and others, 2015; Storch and others, 2023). Unlike a simple beam splitter that guarantees the identical viewing field for two sensors, a field splitter will produce different viewing fields for each of the two sensors (fig. 29). Thus, two EnMAP cameras need to be georeferenced and ortho-corrected individually; therefore, an EnMAP L1C image product that creates a hyperspectral spectrum by combining the two sensors may have a heterogeneous hyperspectral spectrum. If the heterogeneous spectrum indicates that the VNIR and SWIR data georeferencing has a relative error of 1 pixel, then a full hypercube spectrum may have a VNIR spectrum from the pixel; however, the SWIR portion of the spectrum is from the next pixel.

An EnMAP scene from the Mojave Desert (ENMAP01-____L1C-DT0000003185_20220905T191251Z_025_V010401_20240222T085041Z) is used to demonstrate the intersensor georeferencing issue. Over the region, the pixels are locally inhomogeneous as shown in figure 30. Within the spectral overlap region between the VNIR and SWIR camera, which corresponds to 0.9–1.0 micrometer, the two spectra are compared in the magnified plot in figure 30. The spectra from two cameras seem to show that the potential intersensor georeferencing issue was successfully handled.

It is possible to evaluate intersensor georeferencing issues in terms of band to band (B2B) and image to image (I2I). Regarding B2B, it can be determined that the intersensor georeferencing error is about 0.1 pixel, whereas the magnitude of curve jump (discontinuity) from VNIR bands to SWIR bands is just about 0.1 pixel as shown in figures 2 and 3. The I2I differences were calculated for all seven resampled bands for OLI. The I2I scatter plots for all seven bands are shown in figure 31. From left to right and from top to bottom, the scatter plots represent coastal aerosol, VNIR bands (blue, cyan, green, red, and purple), and SWIR bands (purple and black). All scatter plots at the top row are scaled for precise comparison. The first five bands (VNIR) have negligible I2I differences of less than 3 percent of a pixel, but the last two bands (SWIR) are different by 2.6 m. This difference confirms that the intersensor georeferencing error is in the northing direction. The I2I scatterplots along the left column are scaled to reveal the intersensor georeferencing error in the easting direction. Five bands have negligible differences of less than 3 percent of a pixel, and the two SWIR bands show noticeable differences of 3.6 m.

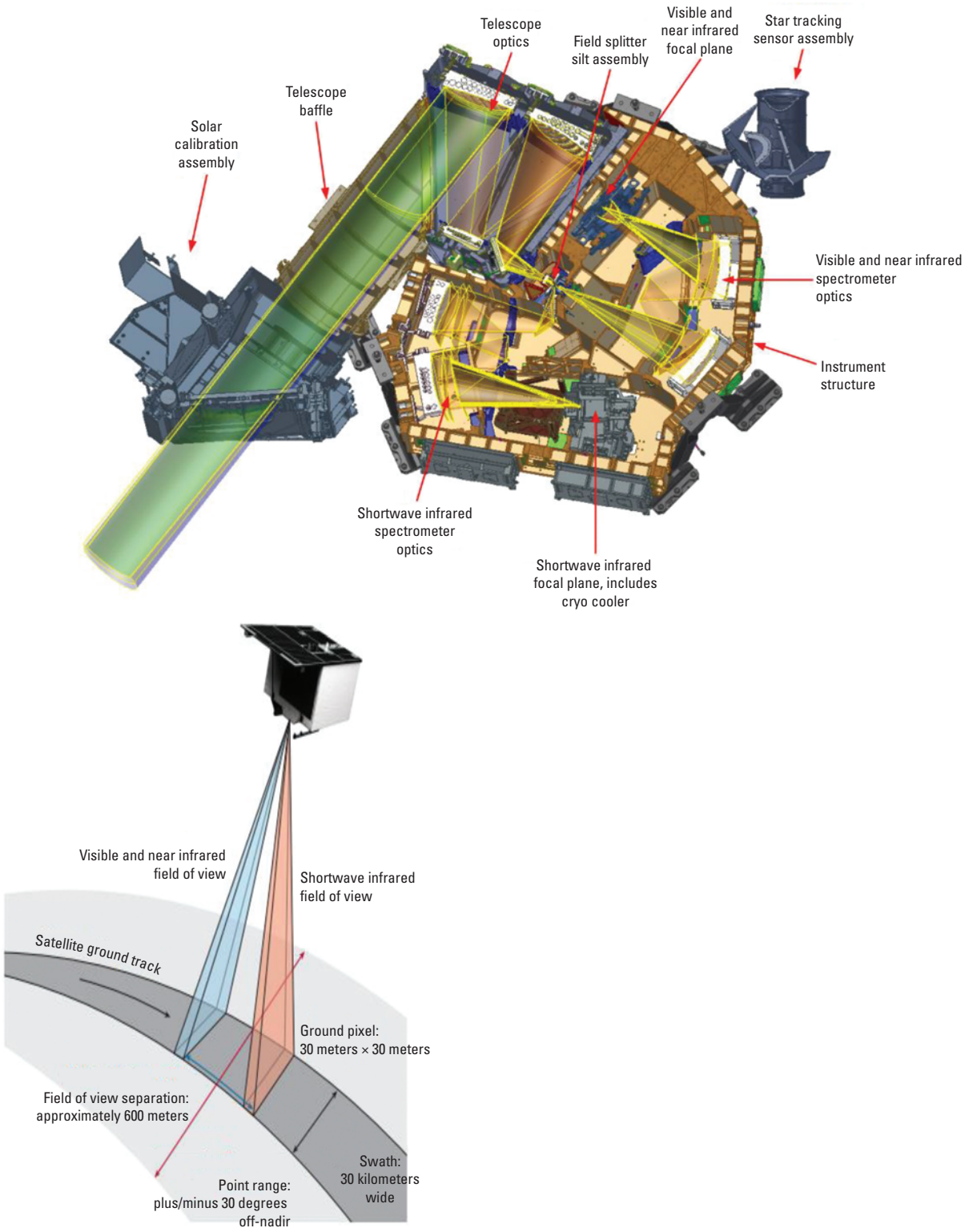

Figure 29. Diagram showing schematic view of the main components of the Environmental Mapping and Analysis Program (EnMAP) and the overpass of two sensors with different viewing fields.

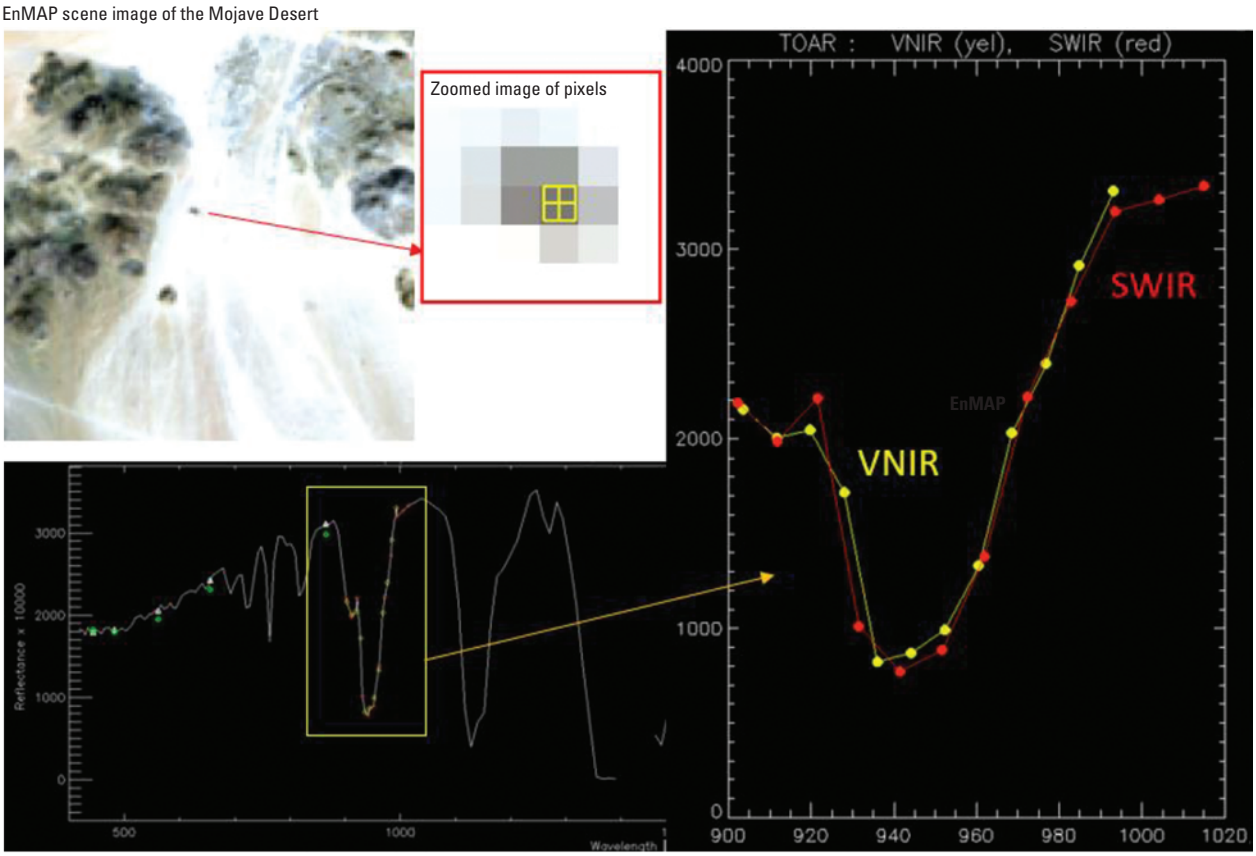

EXPLANATION

EnMAP	**Environmental Mapping and Analysis Program**
VNIR	**Visible and near infrared**
SWIR	**Shortwave infrared**

Figure 30. Graph and image showing an example of heterogeneous hyperspectral spectrum of L1C product image using the Mojave Desert scene (refer to table 6).

I2I differences between VNIR bands and SWIR bands show about 0.1 pixel for both directions (2.6 m in northing, 3.6 m in easting). The middle plot in figure 31 summarizes the mean I2I differences of each EnMAP spectrally resampled bands relative to Landsat OLI (at coordinate origin). Considering the numerical precision of cross-correlation technique, the I2I differences and the B2B differences are almost identical with 0.1 pixel, which demonstrates the quality of the EnMAP georeferencing algorithm and also the consistency of the evaluation algorithm. Georeferencing difference between two independent cameras (although the telescope optics are shared) is about 0.1 pixel.

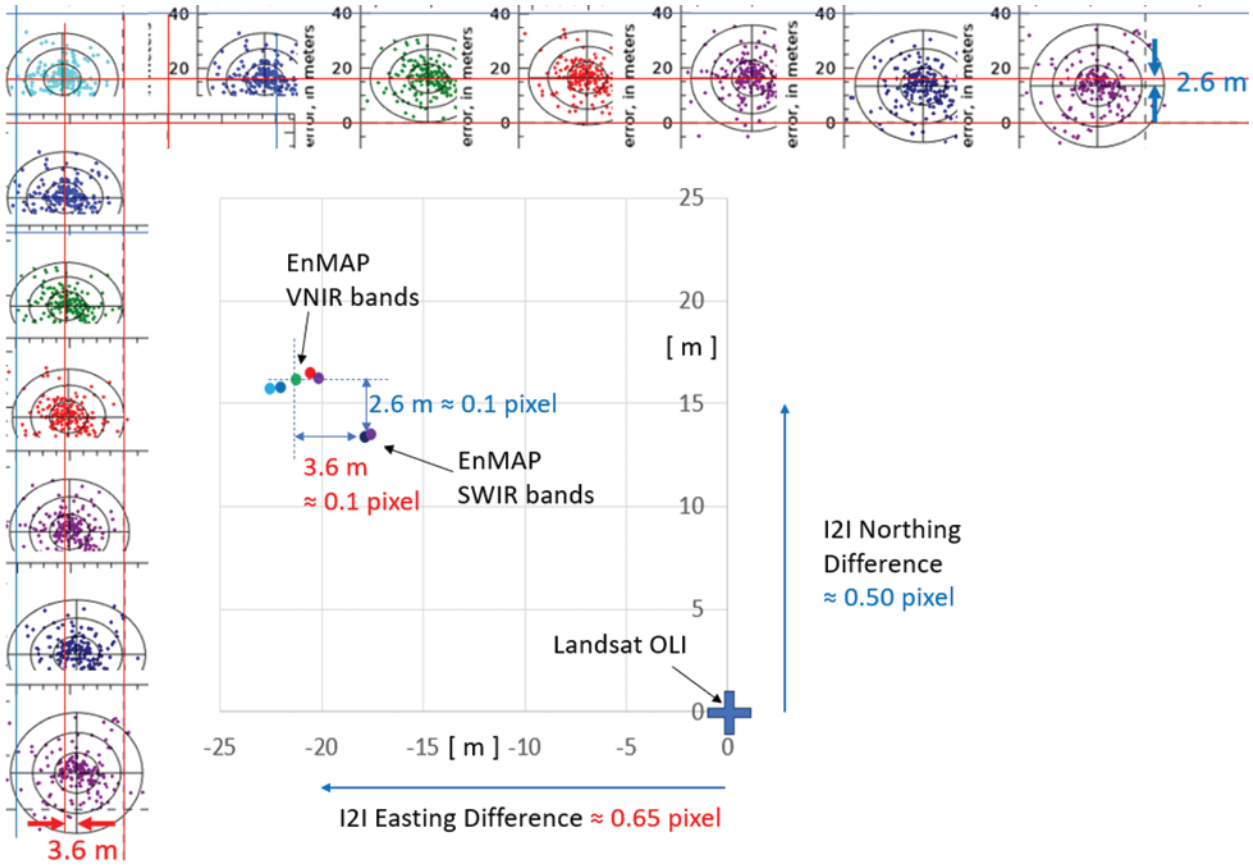

EXPLANATION

EnMAP	Environmental Mapping and Analysis Program
VNIR	Visible and near infrared
SWIR	Shortwave infrared
OLI	Operational Land Imager
m	Meter
≈	Approximately equal

Figure 31. Scatter plot and graph showing image to image evaluation of intersensor error.

Summary and Conclusions

This report summarizes the sensor performance of the Environmental Mapping and Analysis Program (EnMAP) based on the U.S. Geological Survey Earth Resources Observation and Science Cal/Val Center of Excellence (ECCOE) system characterization process. In summary, we have determined that EnMAP has a band-to-band geometric performance in the range of −0.135 to 0.15 pixel, geometric performance relative to the Operational Land Imager in the range of −27.716 meters (−0.92 pixel) to 32.892 meters (1.09 pixels) offset in comparison to Landsat 8 Operational Land Imager, offset of a radiometric comparison in the range of −0.012 to 0.020, slope of a radiometric comparison in the range of 0.947 to 1.031.

In conclusion, the team has completed an ECCOE standardized system characterization of the EnMAP hyperspectral sensor. Although the team followed characterization procedures that are standardized across the many sensors and sensing systems under evaluation, these procedures are customized to fit the individual sensor as was done with EnMAP. The team has acquired the data, defined proper testing methodologies, carried out comparative tests against specific references, recorded measurements, completed data analyses, and quantified sensor performance accordingly. The team also endeavored to retain all data, measurements, and methods. This is key to ensure that all data and measurements are archived and accessible and that the performance results are reproducible.

The ECCOE project and associated Joint Agency Commercial Imagery Evaluation partners are always interested in reviewing sensor and remote sensing application assessments and would like to see and discuss information on similar data and product assessments and reviews. If you would like to discuss system characterization with the U.S. Geological Survey ECCOE and (or) the Joint Agency Commercial Imagery Evaluation team, please email us at eccoe@usgs.gov.

Selected References

Barsi, Lee, K., Kvaran, G., Markham, B., and Pedelty, J., 2014, The Spectral Response of the Landsat-8 Operational Land Imager: Remote Sensing (Basel), v. 6, no. 10, p. 10232–10251. https://doi.org/10.3390/rs61010232.

Cantrell, S.J., and Christopherson, J.B., 2024, Joint Agency Commercial Imagery Evaluation (JACIE) best practices for remote sensing system evaluation and reporting: U.S. Geological Survey Open-File Report 2024–1023, 26 p., accessed August 6, 2024, at https://doi.org/10.3133/ofr20241023.

EnMAP, 2024, Welcome to EnMAP—The German spaceborne imaging spectrometer mission: EnMAP web page, accessed December 30, 2024, at https://www.enmap.org.

Guanter, L., Kaufmann, H., Segl, K., Foerster, S., Rogass, C., Chabrillat, S., Kuester, T., Hollstein, A., Rossner, G., Chlebek, C., Straif, C., Fischer, S., Schrader, S., Storch, T., Heiden, U., Mueller, A., Bachmann, M., Mühle, H., Müller, R., Habermeyer, M., Ohndorf, A., Hill, J., Buddenbaum, H., Hostert, P., Van der Linden, S., Leitão, P., Rabe, A., Doerffer, R., Krasemann, H., Xi, H., Mauser, W., Hank, T., Locherer, M., Rast, M., Staenz, K., and Sang, B., 2015, The EnMAP spaceborne imaging spectroscopy mission for Earth observation: Remote Sensing (Basel), v. 7, no. 7, p. 8830–8857. https://doi.org/10.3390/rs70708830.

Storch, T., Honold, H.-P., Chabrillat, S., Habermeyer, M., Tucker, P., Brell, M., Ohndorf, A., Wirth, K., Betz, M., Kuchler, M., Mühle, H., Carmona, E., Baur, S., Mücke, M., Löw, S., Schulze, D., Zimmermann, S., Lenzen, C., Wiesner, S., Aida, S., Kahle, R., Willburger, P., Hartung, S., Dietrich, D., Plesia, N., Tegler, M., Schork, K., Alonso, K., Marshall, D., Gerasch, B., Schwind, P., Pato, M., Schneider, M., de los Reyes, R., Langheinrich, M., Wenzel, J., Bachmann, M., Holzwarth, S., Pinnel, N., Guanter, L., Segl, K., Scheffler, D., Foerster, S., Bohn, N., Bracher, A., Soppa, M.A., Gascon, F., Green, R., Kokaly, R., Moreno, J., Ong, C., Sornig, M., Wernitz, R., Bagschik, K., Reintsema, D., La Porta, L., Schickling, A., and Fischer, S., 2023, The EnMAP imaging spectroscopy mission towards operations: Remote Sensing of Environment, v. 294, p. 113632, 20 p. https://doi.org/10.1016/j.rse.2023.113632.

U.S. Geological Survey, 2020, EROS CalVal Center of Excellence (ECCOE): U.S. Geological Survey web page, accessed March 2021 at https://www.usgs.gov/core-science-systems/eros/calval.

U.S. Geological Survey, 2025, Landsat Satellite Missions: U.S. Geological Survey web page, accessed February 13, 2025, at https://www.usgs.gov/landsat-missions/landsat-satellite-missions.

For more information about this publication, contact:
Director, USGS Earth Resources Observation and Science Center
47914 252nd Street
Sioux Falls, SD 57198
605–594–6151

For additional information, visit: https://www.usgs.gov/centers/eros

Publishing support provided by the
Rolla Publishing Service Center

ISSN 2331-1258 (online)
https://doi.org/10.3133/ofr20211030s